Study of charge-carrier injection and transport in organic light-emitting diodes

Sang-Geon Park

Contents

Chapter 1Introduction

1-1 Introduction and current state of organic light-emitting diodes

Organic light-emitting diodes (OLEDs) present electroluminescence emissions through the recombination of electron-hole pairs. OLEDs have several advantages, such as light-weight, thinness, low driving voltage, and high contrast ratio. Since OLEDs can be used as a flexible display like plastic, it will be an important technology to replace existing displays in future.

OLED technologies have been constantly evolving through the efforts of numerous researchers. The first observation of electroluminescence in organic materials was in a single crystal of anthracene with electrodes and an external kV-order bias in 1965. However, there were no practical applications of the organic electroluminescence because of extremely high operation voltage (~100V) [1]. In 1987, Tang *et al*. reported a device with organic fluorescent materials. This device consists of function-separated organic layers: carrier-transport andlight-emission layers. OLED was obtained at luminance over 1000 cd/m^2 with a driving voltage of less than 10 V [2]. Adachi *et al.* reported OLEDs with N,N'-diphenyl-N,N'-(3-methylphenyl)-1,1'-biphenyl-4,4'-
-diamine (TPD) as a hole transport layer. The TPD layer is an well-known organic conductor with a high hole mobility of 10^{-3} cm^2/Vs. The observed threshold voltage in EL emission was about 10V. A stable steady current of more than 1 mA/cm^2 was observed at a high voltage of 60V [3]. In addition, Van Slyke *et al.* reported that the performance of OLED can be enhanced by an inserted hole injection layer (HIL) between an anode and a hole transport layer. OLED with the inserted HIL structure showed an operational half-lifetime of about 4000 h from the initial luminance at 510 cd/m^2. The luminance of 1000cd/m^2 was achievable at a driving voltage of 12.8V [4]. This shows the importance of hole injection layer.

In general, inorganic materials are stabler than organic materials around 100 °C. Especially

diamine derivatives as TPD have a low glass transition point, i.e. that of TPD is ~60 °C. Therefore, the hybrid of inorganic and organic materials has been studied. Tokito *et al.* reported the MgF_2 doped TPD as HTL in OLEDs [10]. In OLEDs with the MgF_2(21 vol %) containing a TPD layer, light emissionscan be measured from 6 V and a high luminance of 2600 cd/m^2 is achieved at a current density of 240 mA/cm^2 with a driving voltage of 15 V [5].

OLED technologies have been growing to the present time not only in academic researches, but also in OLED related industries. The global OLED market size became almost $4 billion in 2011 [5]. It is expected that the market will continue to grow over $35 billion by 2018, a compound annual growth rate (CAGR) of ~40% [6]. Market demands of OLED materials have also increased. The total market size in OLED materials will grow from about $450 million in 2013 to over $4.6 billion by the end of the decade. Leading OLED materials suppliers are Universal Display, DuPont, Cheil, Novaled, and Sumitomo [7].

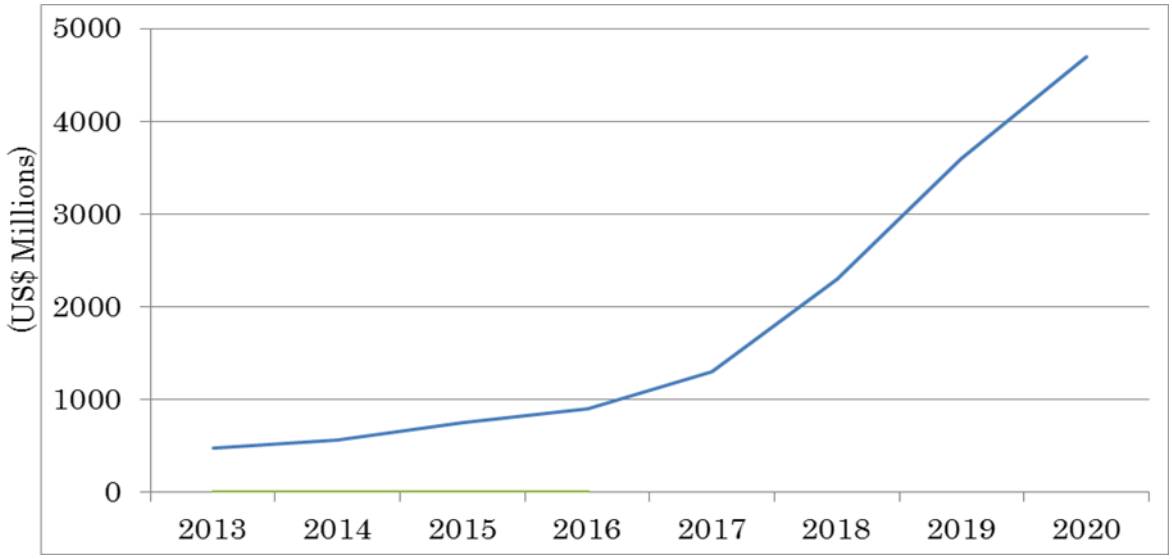

Figure 1-1 Grand Total Summary: Market Values in OLED materials [7].

OLED lighting businesses in OLED markets are also growth [6]. Several manufacturers have already begun to launch commercial OLED lighting products on the market. Philips, Osram,

Panasonic, and Lumiotec are the world's most progressive developers of OLED lighting products. OLED technologies have been growing rapidly in the related industries such as material and lighting. OLEDs have emerged as the next-generation lighting. This is chiefly because OLED is solid-state lighting technology, and as such is capable of meeting the requirements of next-generation lighting in terms of improved color rendition. For example, OLEDs can enable a high contrast ratio compared to liquid crystal displays (LCD) because OLED pixels directly emit light. However, only a small number of OLED lighting products are currently available on a commercial basis. The main technical problem for OLEDs is the limited lifetime of the organic materials. For example, blue OLEDs have had a lifetime of around 14,000 hours to half original brightness. This is lower than the typical lifetime of LCD. Studies of charge carrier injection – transport are keysto low driving voltage. Therefore, improvement of charge-carrier injection and transport in OLEDs are studied in this work.

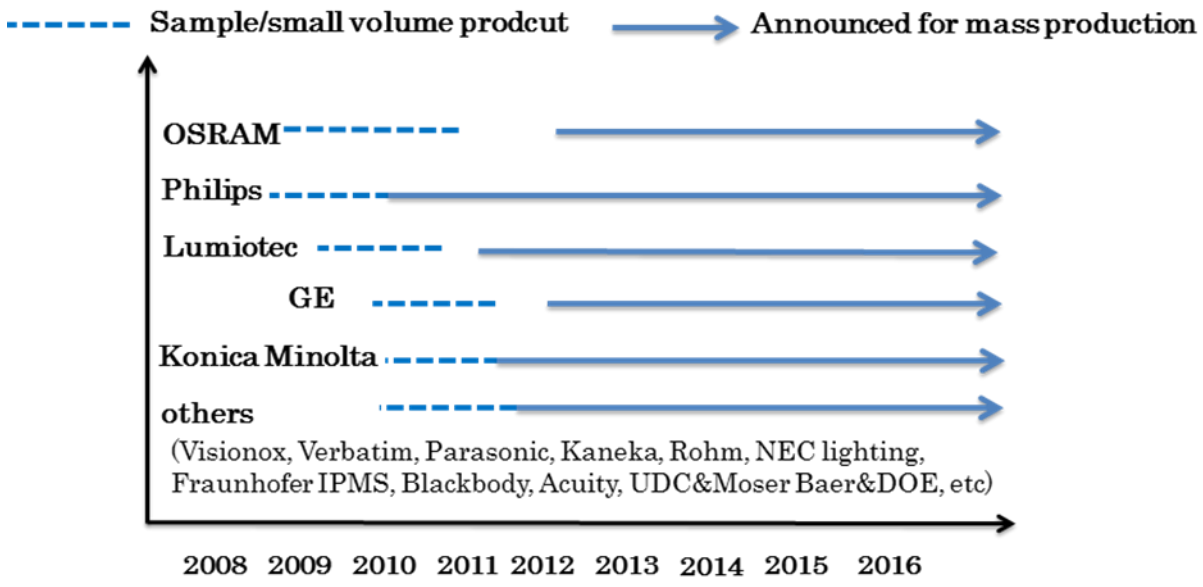

Figure 1-2 OLED Lighting Long-Term Annual R & D Forecast [6].

1-2 Electrical conduction and light-emitting mechanism of OLED

Typical OLED consists of several different layers; a hole injection layer (HIL), a hole transport layer (HTL), an emission layer (EML), an electron transport layer (ETL), and an electron injection layer (EIL) as shown in Figure 1‑3.

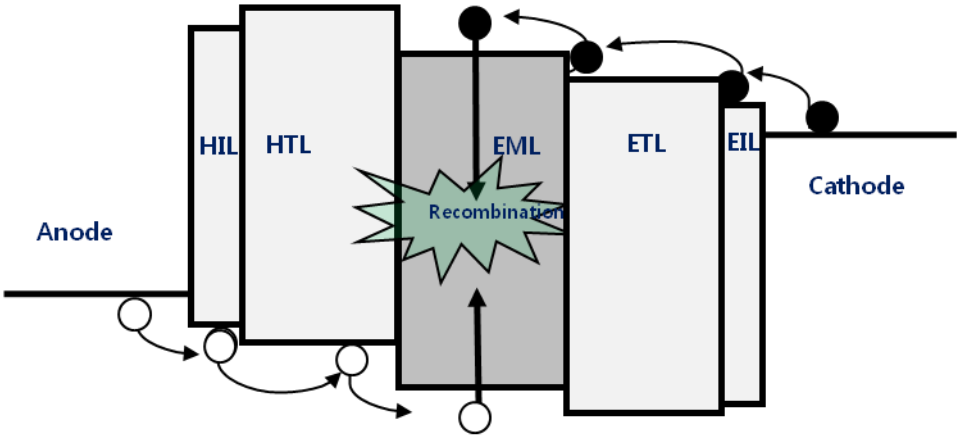

Figure 1-3 Emission mechanism of multi-layer type OLED.

In inorganic semiconductors, the paths of electrons and holes are called conduction and valence bands, respectively. In organic materials, each path represents either a lowest unoccupied molecular orbital (LUMO) or a highest occupied molecular orbital (HOMO). In general, when those are described by a band model, the HOMO level of an organic material is located at the ionization potential (Ip) below the vacuum level. The LUMO level is equivalent to the electron affinity (χ). As shown in Figure 1-4, the term of Ip can be directly measured by an ultraviolet photoelectron spectroscopy (UPS) but χ cannot be measured but can be almost estimated from $\chi = I_p - E_g$.

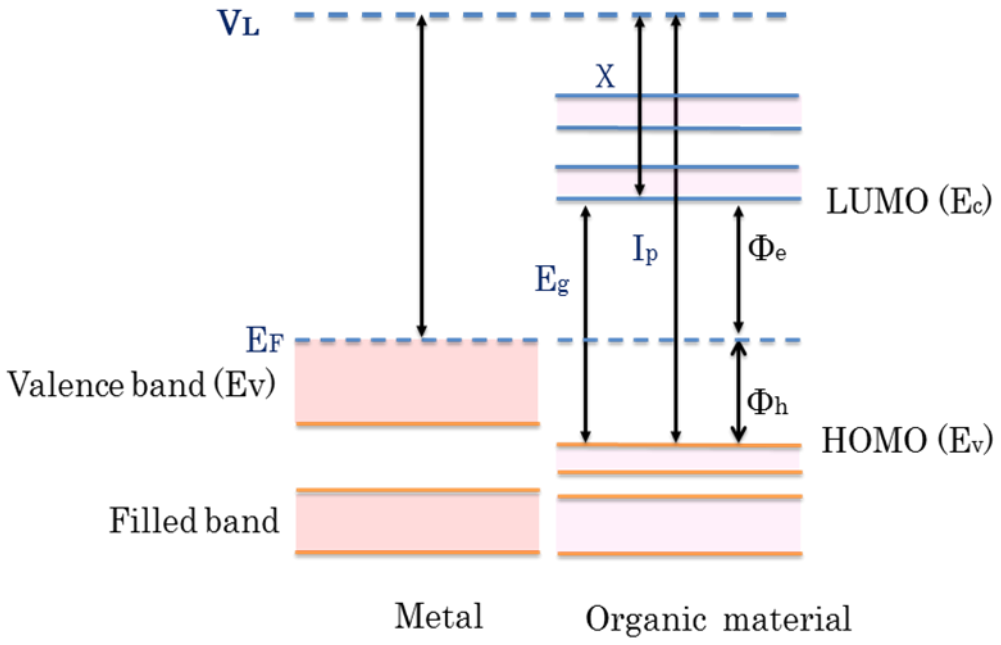

Figure 1-4 Energy levels of metal and organic material (Φe, Φh: electron and hole injection barriers, Eg : energy gap).

•Emission mechanism

The emission of light is the final process in OLEDs. If holes and electrons meet on an organic molecule, an electron - hole pair will recombine and the molecule will become excited. The excited states are known as ‘exciton’. The exciton emits light when the excitation is deactivated.

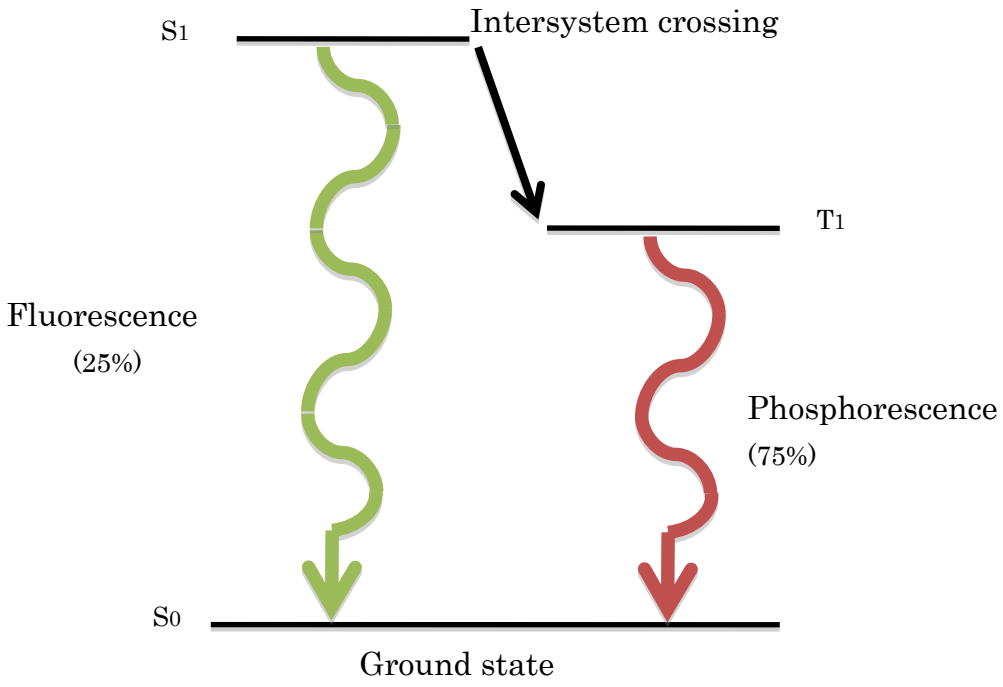

Figure 1-5 Energy diagram of fluorescence and phosphorescence.

Figure 1-5 shows an energy diagram of fluorescence and phosphorescence. The density of singlets and triplets will be produced as 25 and 75 % on carrier recombination. According to quantum mechanics, the radiative relaxation from the triplet state to the ground state is forbidden. The complete crossing phosphorescent OLEDs can be used on both singlet and triplet excitons to realize a theoretical internal quantum efficiency of 100%. Ordinarily, the phosphorescence materials are used as a light emitting material, such as Tris[2-phenylpyridinato-C2,N]iridium(III) (Ir(ppy)3), Bis[2-(4,6-difluorophenyl)pyridinato-C2,N](picolinato)iridium(III) (FIrpic), and Platinum octaethylporphyrin (PtOEP). These phosphorescent materials enhance the energy transfer from the host singlet and triplet states to the guest triplet state through intersystem crossing.

The external quantum efficiency, η_{ext}, of OLED is described as the follow:

$$\eta_{ext} = a \cdot \eta_{int} = a \cdot \varphi_{PL} \cdot \varphi_{exciton} \cdot \gamma_r \quad \ldots (1.1)$$

where a is out-of-coupling of light factor, η_{int} is the internal quantum efficiency of OLED, ϕ_{PL} is the photoluminescence (PL) quantum yield, ϕ_{exciton} is an exciton generation factor of an electron-hole pair, γ is the carrier balance factor. The γ is defined as the ratio of the current density of carrier recombination to the total current density flowing in external circuit. If the supplied current density distributes to carrier recombination, the γ is a unity and the maximum. The ϕ_{exciton} is defined by the chemical quantum mechanics, 0.25 for fluorescence and 0.75 for phosphorescence. Especially the ϕ_{exciton} of the complete crossing phosphorescence is a unity and the maximum. Although the ϕ_{PL} depends on an organic material, its maximum is a unity. Consequently if the materials and device structure are optimized, the η_{int} will be able to obtain the maximum and a unity. In general, the a is 0.2-0.3 (no optical design) and >0.4 (an optimal optical design). The η_{ext}, of electrically and optically optimized OLED is controlled by the out-of-coupling of light factor. To realize the high-performance OLED, it is important to develop excellent materials and design the device structure. From the viewpoint of energy, the energy efficiency, η_{e} of OLEDs under applying a voltage, V is described by

$$h_e = h_{\text{int}} \frac{E_{photon}}{eV}, \qquad \ldots (1.2)$$

where e is the elementary charge, eV is the input energy and E_{photon} is the average energy of emitted photons. This means that the increase in η_{e} depends on the decrease in applied (operating) voltage. Since organic materials are essentially insulating materials, the enhancement of carrier injection and the increase in conductivity are important to reduce the operating voltage.

•Carrier Injection

Charge injection is the process of promoting electrons or holes from an electrode to the HOMO or LUMO in the organic layers of OLEDs. Ideally, the anode should have a higher work function than the HOMO of the HTL, which leads to lower barrier height of hole injection, depending on the energy difference between the work function of the anode and the HOMO of HTL. HIL can enhance the hole injection from anode to HTL. In addition, HIL improves the smoothness of the electrode surface e.g. the bare rough ITO. HIL reduces the probability of electrical shorts [8]. The easier carrier injection leads to the lower operating voltage. The small input energy will be obtained by the low operating voltage under a constant current density. Therefore, it is important to improve the carrier injection.

•Conduction

Electrical conduction in organic materials depends on the carrier injection and charge transport. As previously mentioned, the carrier injection is important and affected by a proper design in an interface between anode and organic materials. A charge transport mechanism is also an important factor that governs the performance of OLEDs. The primary factor in the charge transport is the carrier mobility. The typical mobility in organic materials used in OLEDs is between 10^{-3} and 10^{-7} $cm^2/V{\cdot}s$. When the carrier injection rate is high enough, the currents inorganic materials are often limited by the charge transport in organic layers. This current limit is called the Space Charge Limited Current (SCLC). I introduce SCLC model.

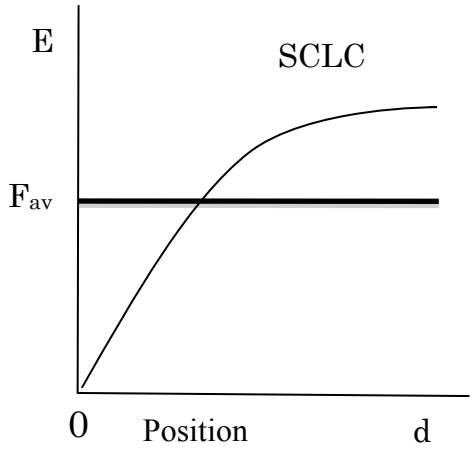

Figure 1-6 Electric field distribution in a device for SCLC [9].

In Figure 1-6, F_{av} is the average electric field, i.e. the applied voltage V divided by a sample film thickness d. As shown in Figure 1-6, the electric field at the electrode becomes weaker due to space electric charge whose polarity is the same as that of the electrode. On the contrary, the electric field at the opposite electrode becomes stronger due to the counter space charge [9]. The derivation of SCLC is as follows:

We consider a thin film with two electrodes. The thickness of the thin film is d. The direction of thinness is x direction. The positions of the anode and cathode are defined as 0 and d, respectively. The electric field and carrier density at the position of x are $E(x)$ and $n(x)$, respectively. The current density J of thin film is presented as

$$J = e\mu n(x)E(x), \qquad \ldots(1.3)$$

where μ is the carrier mobility and e is an electric charge.

The Poisson equation can be written as

$$\frac{dE(x)}{dx} = \frac{en(x)}{\varepsilon}, \qquad \ldots(1.4)$$

where ε is permittivity.

Substituting (1.3) to (1.4),

$$J = e\mu \frac{dE(x)}{dx} \frac{\varepsilon}{e} E(x), \qquad \ldots (1.5)$$

$$J = e\mu E(x) \frac{dE(x)}{dx}, \qquad \ldots(1.6)$$

Solving the differential equation (1.4),

$$\int J\,dx = \int e\mu E(x)\,dE(x), \qquad \ldots(1.7)$$

If we assume E(0) = 0, the integral equation (1.7) from 0 to x can be presented as

$$J \cdot x = \frac{1}{2} \varepsilon\mu E(x)^2, \qquad \ldots(1.8)$$

Then, the electric field is described as

$$E(x) = \sqrt{\frac{2J}{\varepsilon\mu}} \cdot x^{\frac{1}{2}}, \qquad \ldots(1.9)$$

Integrating both sides of Equation (1.9) on x,

$$\int E(x)dx = \sqrt{\frac{2J}{\varepsilon\mu}} \int x^{\frac{1}{2}} dx, \qquad \ldots(1.10)$$

The applied voltage can be calculated by an integral of the electric field from 0 to d.

$$V = \int_0^d E(x)dx = \frac{2}{3}\sqrt{\frac{2J}{\varepsilon\mu}}d^{\frac{3}{2}}, \qquad \ldots(1.11)$$

Solving the Equation (1.11) for J, the current density of trap free SCLC is described as

$$J = \frac{9}{8}\varepsilon\mu\frac{V^2}{d^3}, \qquad \ldots (1.12)$$

.

As shown above, the current density of SCLC is proportional to V^2 and d^3. This is the trap-free SCLC current density.

Figure 1-7 shows a schematic log-log plot of the current density-voltage characteristics from ohmic to space charge limited conduction. Currents are proportional to the voltage ($J \propto V$) in the low voltage region. In this region, carriers injected from an ohmic interface can be transported easily. Increasing the carrier injection in a higher voltage region, the carrier transport is shifted to SCLC ($J \propto V^2$).

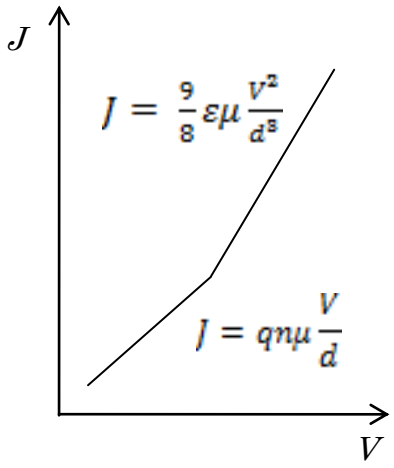

Figure 1-7 Schematic log-log plot of the current density-voltage characteristics from ohmic to space charge conduction.

1-3 Purpose and scope of this study

As shown in the research of organic field effect transistors, the conductivity of an organic material strongly depends on the carrier injection from an electrode. Lower operating voltage for OLEDs can be realized by improving the carrier injection from electrodes. First I tried to improve hole injection using a hole injection material, self-assembled monolayer (SAM) and optimized the molecular structure of fluorinated SAM. Second I tried to develop a stabler organic-inorganic hybrid hole injection layer for OLEDs using molybdenum oxide.

1-3-1 Optimization of fluorinated SAM

SAM is a molecular assembly formed spontaneously on substrate surfaces and is organized into more or less large ordered domains. SAM layers consist of a bond part, an alkyl chain section, and an end functional group. Hole injections in OLEDs can be changed by using SAM to modify an energy level offset at an interface of ITO/HTL. SAM provides a method of tuning the work function

of an anode to the HOMO level of HTL [10].

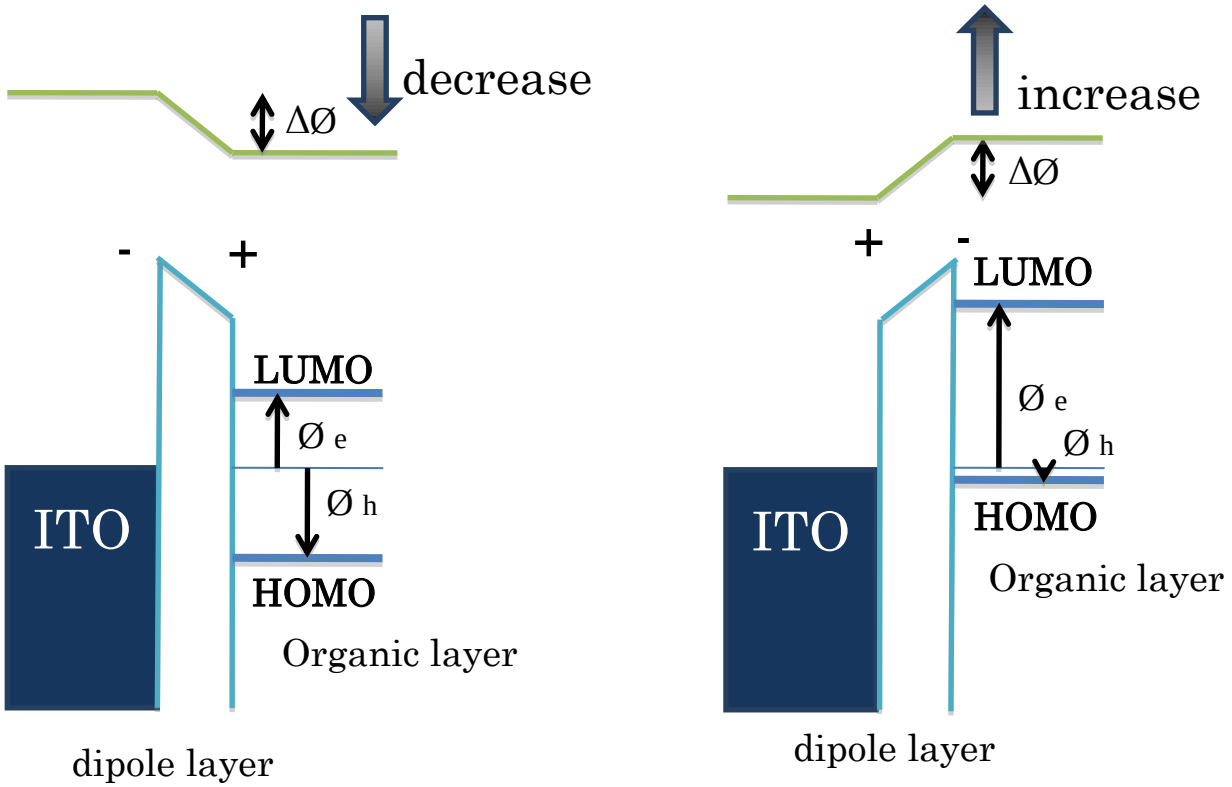

Figure1-8 Diagram of energy shifts caused by interfacial dipole layers: Left, the right-dipole direction (decreases in the vacuum level(V_L)); Right, the left-dipole direction (increases in V_L) ; $\Delta\phi$, the shifts of V_L, ϕ_e and ϕ_h, the barrier heights of electron and hole, respectively.

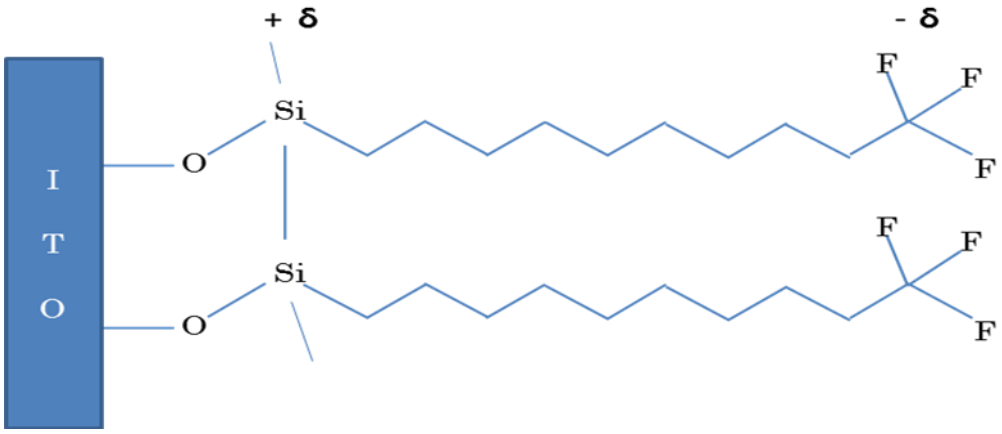

Figure 1-9 Dipole polarity of the FSAM on the ITO substrate.

The interfacial dipole formed by SAM can change vacuum levels. Figure 1-8 shows the effects of the interfacial dipole layer. The value and direction of the interfacial dipole moment affect vacuum level shifts. In the left case, the barrier height of the hole injection from ITO to an organic layer will be increased by lowering the vacuum level in organic layer and then the hole injection from ITO will also be suppressed. In the right case, the barrier height of the hole injection from ITO to an organic layer will be decreased by raising the vacuum level in organic layer and then the hole injection from ITO will be enhanced. The interface dipole effect of FSAM molecules is caused by the strong electronegativity of fluorine atoms. As shown in Fig. 1-9, the dipole moment of FSAM molecule is the direction from F atoms to the ITO substrate. This is the right case of Fig. 1-8. Therefore, the device of FSAM-modified ITO can promote hole injections.

Mori *et al.* investigated the driving voltages among HIL with or without FSAM, CuPc, and CH_3SAM [11,12]. The device structure consisted of ITO(anode)/HIL(without or FSAM, CuPc, CH_3SAM)/α-NPD (50nm, HTL)/Alq3(50nm, EML and ETL)/LiF(EIL)/Al(cathode). The driving voltage of the device with FSAM, CuPc, CH_3SAM, and without HIL at 10^{-2} A/cm^2 were estimated to be approximately 5, 7,15, and 14.5V, respectively. Driving voltages in a device with FSAM represent the lowest value among the used HILs owing to the lowest barrier height of the hole injection from ITO to HTL. A device of FSAM is achieved with a driving voltage of 8.8 V after 100 h. However, a device of CuPc is achieved with a driving voltage of 12 V after 100 h. The driving voltage for the OLED with FSAM is found to be smaller than that of the OLED with CuPc. It is considered that the use of FSAM as HIL is effective for improving the stability of OLEDs according to the low driving voltage.

As described above, it is very effective to use FSAM as a hole injection layer. The shift of vacuum level depends on the value of interface dipole moment. If the fluorinated alkyl chain of FSAM is prolonged, it is thought that a larger polarization of molecule will be realized. On the other hand, since the alkyl chain is an insulating part, prolonging an alkyl chain is thought to affect

the carrier transfer between ITO and α-NPD.

On the alkyl chain length of SAM, Hozumi et al. reported the characteristics of SAM molecules with various alkyl chain lengths [13]. As the alkyl chain length increases, the contact angle of a substrate surface also increases owing to the hydrophobic characteristics of SAM molecules. Therefore, SAM molecules with a long alkyl chain have a large contact angle [14]. Tao *et al.* investigated the characteristics of SAMs with different chain lengths. There is a little difference between the HOMO energy level and the work function of the SAM-modified anode in the case that α-NPD as HTL is used in which the carrier injection is modulated by the alkyl chain length of the used SAM (tunneling distance-dependent). The carrier injection is decreased by increasing the alkyl chain lengthbecause of the insulating characteristics of SAM [15]. Therefore, it is necessary to optimize the alkyl chain length of FSAM.

1-3-2 Organic-inorganic hybrid using MoOx

MoOx has been used as a hole injection material in OLEDs. For the first time, Tokito *et al.* investigated metal oxides such as MoOx, VOx and RuOx as HIL for OLEDs [15]. They found decreases in driving voltages by using the metal oxide layer as HIL for OLEDs. Moreover, they found a relationship between the work function of the metal oxides and the driving voltage. The reduction of the driving voltage was attributable to the lower energy barriers of the metal oxide/HTL interfaces compared to that of the ITO/HTL. You *et al.* reported that the driving voltage at 1000 cd/m^2 was 6.9 V and that the turn-on voltage (defined as a voltage at 1 cd/m^2) was 2.4 V [16]. Yook and Lee also reported that the driving voltage at 1,000 cd/m^2 was reduced from 8 V to 6.7 V by using the MoOx layer [17]. As mentioned above, MoOx is a promising material for HTL in improving the performance of OLEDs [17].

MoOx shows the influences of charge transfer with an organic material as an

organic-inorganic hybrid system. Matushima *et al.* reported that an enhancement in the current density of the device of α-NPD by using a MoOx layer provided the evidence of the charge transfer effect [18]. Shin *et al.* reported the charge transfer effect of α-NPD and MoOx by co-evaporation. The current density–voltage characteristics with the MoOx-doped layers at two different MoOx concentrations, 5% and 10%, were investigated. The driving voltage accompanied with the increases in MoOx concentrations decreased from 10.2 Vto 8.4 V at a fixed current density of 100 mA/cm^2. The driving voltage showed low MoOx concentrations, such as 5% and 10% [19].

Kröger reported a study on p-type doping of organic materials with MoOx. The charge transfer by the co-evaporation of MoOx and α-NPD can increase carrier densities [20]. Figure 1-10 shows the energy diagram of MoOx and α-NPD thin films from the UPS measurement [20,21,22]. The Fermi level (6.9 eV) is close to the conduction band (6.7eV) for MoOx [20,21]. The Fermi level (4.8 eV) is close to the HOMO level (5.4 eV) for α-NPD. Yi *et al.* reported that electrons can be directly transferred from the HOMO level of α-NPD to the conduction band of MoO_x [21]. That is, holes are transferred to the HOMO level of α-NPD. The charge transfer complex is formed at the interface between α-NPD and MoOx.

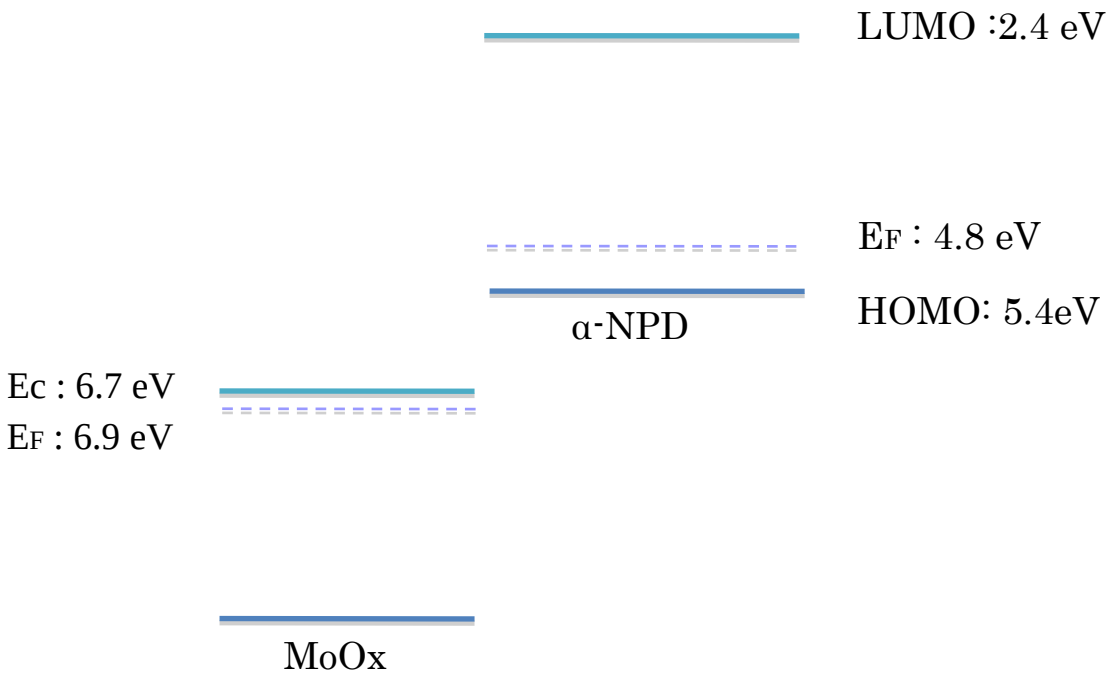

Figure 1-10 Energy levels of MoOx and α-NPD [20,21,22].

Figure 1-11 shows the energy level alignment of co-evaporation from UPS measurement. Kröger *et al*. reported by UPS measurement that the Fermi levels of the co-evaporation thin film is located approximately 0.44 eV above the HOMO level and that the location of the Fermi level depends on MoOx concentration [22].

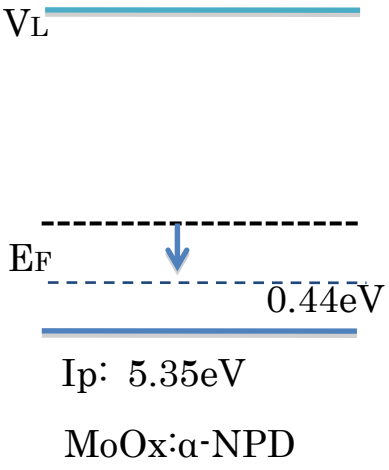

Figure 1-11 Energy levels by co-evaporation of MoOx and α-NPD [22].

Figure 1-12 shows the energy difference between the Fermi and HOMO levels vs. the MoOx doping concentration in α-NPD films on the ITO substrate. As the MoOx doping concentration of co-evaporation thin film is increased, the difference between the Fermi level of co-evaporation thin film and the HOMO level decreases. When α-NPD is co-evaporated with MoOx, a significant increase in conductivity is observed compared to α-NPD thin films by the charge transfer [22].

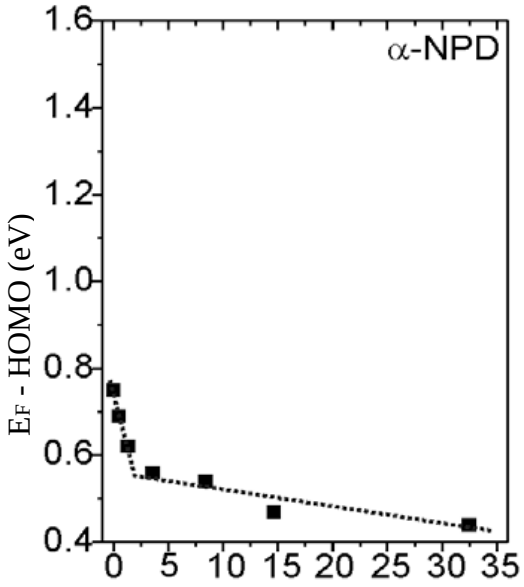

Figure 1-12 Energy difference between the Fermi (the dopant and host are MoOx and α-NPD respectively) and HOMO levels (the dopant and host are MoOx and α-NPD respectively) vs. the MoOx doping concentration in α-NPD films on the ITO substrate [22]

\

As previously mentioned, co-evaporation thin film of MoOx:α-NPD improve performance. The purpose of this research (Chapter 4) is to study improvement of the charge carrier injection and transport in the co-evaporation thin film of MoOx in OLEDs.The influencesof co-evaporation on both interface and electrical characteristics are investigated.

1-4 Composition of this thesis

This is composed of five chapters. They are listed below.

Chapter 1 is the introduction and describes the introduction, electrical conduction, and emission mechanism of OLED are introduced. Also, the objective of this paper is discussed.

In Chapter 2 device fabrication and evaluation methods are reviewed.

In Chapter 3 the effects of the interface control and electrical characteristics of FSAMs with various alkyl chain lengths as HIL in OLED are investigated. The dipole moment, contact angle, and work function for evaluating the interfacial properties of FSAMs with various alkyl chain lengths are investigated. The current density-voltage and EL intensity-wavelength characteristics for evaluating the electrical properties of FSAMs with various alkyl chain lengths are investigated. The reason of enhancing the current density by FSAMs with the insulating film characteristics of alkyl chains is discussed.

In Chapter 4, the effects of the structural and electrical characteristics of the co-evaporation thin film of MoOx:α-NPD as HIL in OLED are investigated. The work function, transmittance, and AFM image for evaluating the film properties of the co-evaporation thin film of MoOx:α-NPD, the current density-voltage and EL intensity-wavelength characteristics for evaluating the electrical optical properties of the co-evaporation thin film and their temperature dependence characteristics are investigated.

Chapter 5 summarizes the issue discussed in this thesis and future challenges in this field.

References

[1] W. Helfrich and G. Schneider, “Recombination Radiation in Anthracene Crystals”, Phys. Rev. Lett. **14** (1965) 229.

[2] C. W. Tang and S. A. VanSlyke, “Organic electroluminescent diodes”, Appl. Phys. Lett. **51** (1987) 913.

[3] C. Adachi, S. Tokito, T. Tsutsui and S. Saito, “Electroluminescence in Organic Films with Three-Layer Structure, ”Jpn. J. Appl. Phys. **27** (1988) 269.

[4] S. A. Van Slyke, C. H. Chen and C. W. Tang, “Organic electroluminescent devices with improved stability,” Appl. Phys. Lett. **69** (2160) 1996.

[5] S. Tokito and Y. Taga, “Organic electroluminescent devices fabricated using a diamine doped MgF_2 thin film as a hole-transporting layer”, Appl. Phys. Lett. **66** (1995) 6.

[6] J. Colegrove, “OLED Display and OLED Lighting: Technologies and Market Forecast”, DISPLAYSEARCH an NPDGroup company (2012).

[7] R. Nolan, “Grand Total Summary: Market Value of OLED materials”, Nano market (2013).

[8] A. Kitai, “Principle of Solar Cells, LEDs and Diodes: The role of the PN junction”, John Wiley & Sons, Ltd. (2011).

[9] T. Mori “Guidebook of easy OLED”, Nikkan Kogyo Shimbun (2008) P.47. (in Japanese).

[10] Editorial department, “LighTimes: New ‘Fluorescent’ Material Has Over 90% Internal Quantum Efficiency”, Optronic Laboratories, Inc. (2013).

[11] T. Mori, M. Imanishi and T. Nishikawa, “Electrical Conduction of Organic Light-Emitting Diodes Using Self-Assembled Monolayer-Modified Indium Tin Oxide Electrode” J. Photopolym. Sci. Technol. **25** (2012) 3.

[12] T. Mori, S. Nishino, T. Nishikawa and S. Ogawa, “Effect of self-assembled monolayer on electroluminescence properties of organic light-emitting diodes”, Jpn. J. Appl. Phys.**47** (2008) 455.

[13] A. Hozumi, K. Ushiyama, H. Sugimura, and O. Takai, “Fluoroalkylsilane Monolayers Formed by Chemical Vapor Surface Modification on Hydroxylated Oxide Surfaces”, Langmuir **15** (1999) 7600.

[14] Y. Tao, K. Wub, K. Huang, and T. Perng, “Odd–even modulation of electrode work function with self-assembled layer: Interplay of energy barrier and tunneling distance on charge injection in organic light-emitting diodes”, Org. Electron. **12** (2011) 602.

[15] S. Tokito, K. Noda and Y. Taga, “Metal oxides as a hole-injecting layer for an organic electroluminescent device”, J. Phys. D: Appl. Phys. **29** (1996) 2750.

[16] H. You, Y. Dai, Z. Zhang, and D. Ma, “Improved performances of organic light-emitting diodes with metal oxide as anode buffer”, J. Appl. Phys. **101** (2007) 026105.

[17] K. Yook and J. Lee, “Low driving voltage in organic light-emitting diodes using MoO_3 as an interlayer in hole transport layer”, Synthetic Metals. **159** (2009) 69.

[18] T. Matsushima, G. Jin, Y. Kanai, T. Yokota, S. Kitada, T. Kishi, and H. Murata, “Interfacial Charge Transfer and Charge Generation in Organic Electronic Devices Organic Electronics”, Org. Electron. **12** (2011) 520.

[19] W. Shin, J. Lee, J. Kim, T. Yoon, T. Kim, and O. Song, “Bulk and interface properties of molybdenum trioxide-doped hole transporting layer in organic light-emitting diodes”, Org. Electron. **9** (2008) 333.

[20] M. Kröger, S. Hamwi, J. Meyer, T. Riedl, W. Kowalsky, and A. Kahn, “Role of the deep-lying electronic states of MoO3 in the enhancement of hole-injection in organic thin films”,Appl. Phys. Lett. **95** (2009) 123301.

[21] Y. Yi, S. Cho, and S. Kang, “Comment on “Observation of space-charge-limited current due to charge generation at interface of molybdenum dioxide and organic layer” ”, Appl. Phys. Lett. **97** (2010)016101.

[22] M. Kröger, S. Hamwi, J. Meyer, T. Riedl, W. Kowalsky and A. Kahn, “P-type doping of

organic wide band gap materials by transition metal oxides: A case-study on Molybdenum trioxide", Org. Electron. **10** (2009) 932.

Chap 2 Experimental methods

2-1 Introduction

The characteristics of OLED are affected by various factors, such as organic material purity, interfacial contamination in organic thin-films, evaporation condition, and evaluation methods. In this chapter, we will mention the fabrication of samples and the evaluation methods.

2-2 Fabrication of samples

2-2-1 Organic materials and fabricated structure in OLEDs

OLEDs are characterized by a multi-layered structure. Figure 2-1 shows a typical structure of OLED used in this study. FSAMs with various alkyl chain lengths and MoOx as HIL, α-NPD as HTL, tris(8-hydroxyquinoline)aluminum(III) (Alq3) as EML, Lithium fluoride (LiF) as EIL, Al as cathode, and ITO and Ag as anode are used. The chemical structures of α-NPD and Alq3 are shown in Fig. 2-2.

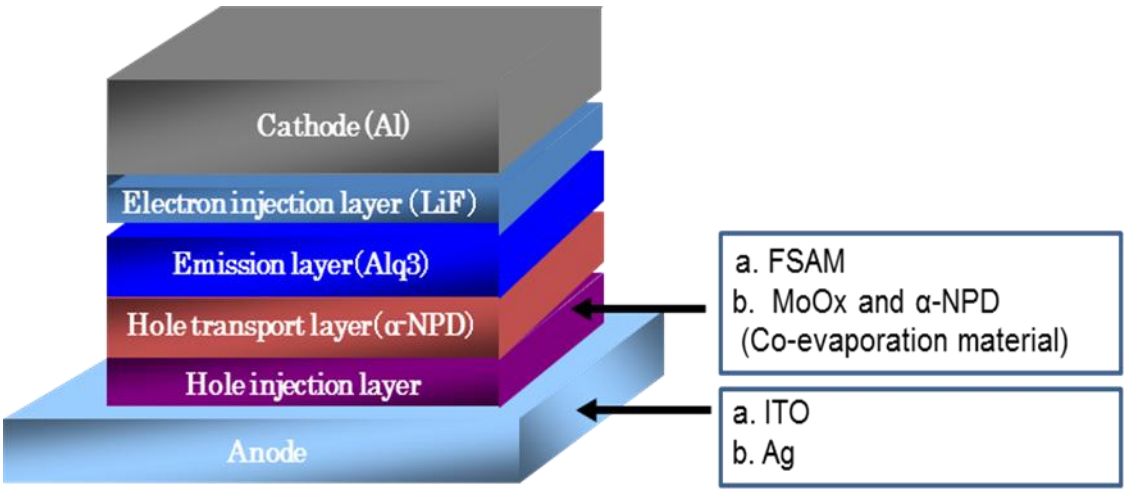

Figur

e 2-1　Structure of OLED.

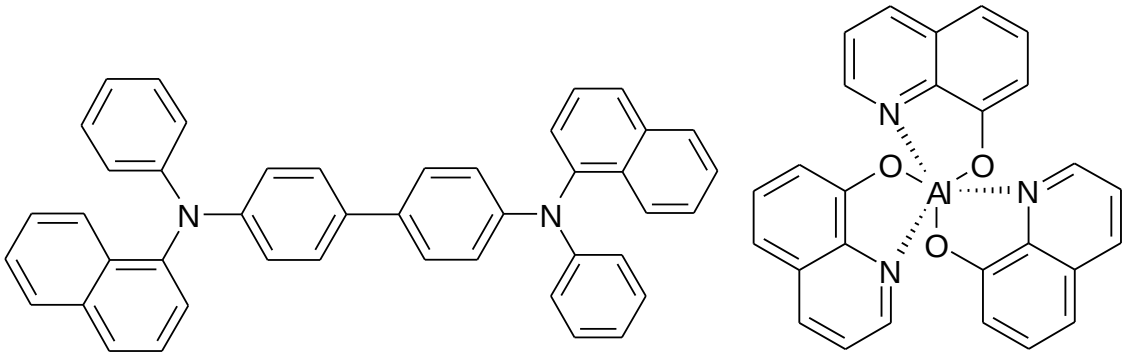

(a) α-NPD　　(b) Alq3

Figure 2-2　Chemical structure of the organic materials used in this study.

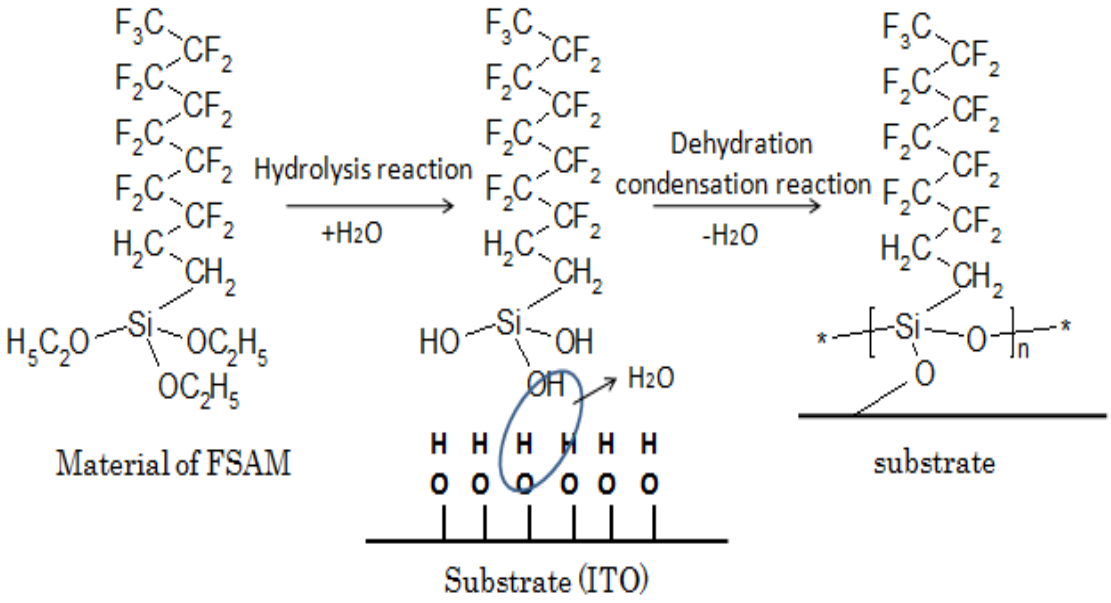

Figure 2-3 FSAM formation.

Figure 2-3 shows the FSAM formation. After the hydrolysis reaction at high temperature, the alkoxy groups change to hydroxyl (-OH) groups. The bonding part of FSAM reacts with the neighboring hydroxyl groups on the ITO substrate. After the dehydration-condensation reaction is completed, the Si atom is linked to the ITO. The FSAM molecules are also linked to the neighboring molecules via the ether group. Then, the FSAM domains are extended repeatedly [1].

Figure 2-4 shows the FSAM chemical structures with various alkyl chain lengths. The lengths of FSAMs are approximately 0.5~1.6 nm. The electronegativities of F and C atoms are 4.2 and 2.5, respectively. Because the difference in the electronegativity between F and C is large, the dipole moment of the F-C group shows a large value.

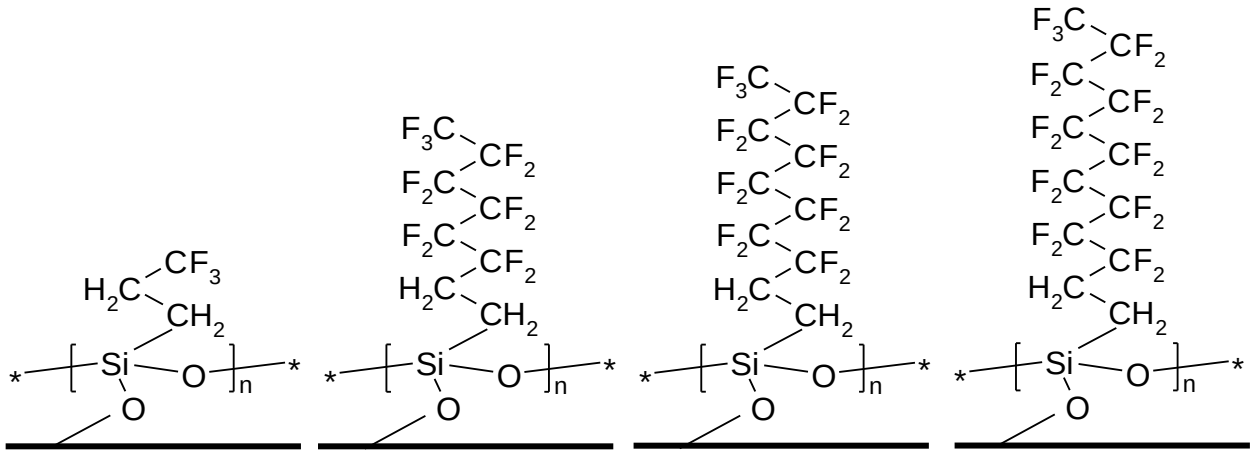

Figure 2-4 Chemical structures of FSAMs with various alkyl chain lengths.

The chemical names of F3SAM, F8SAM, F10SAM, and F12SAM are (3,3,3-trifluoropropyl)-trimethoxysilane($CF_3(CF_2)(CH_2)_2Si(OC_2H_5)_3$), tridecafluoro-1,1,2,2,-tetrahydrooctyltriethoxysilane ($CF_3(CF_2)_5(CH_2)_2Si(OC_2H_5)_3$), heptadecafluoro-(1,1,2,2-tetrahydrodecyl)triethoxysilane ($CF_3(CF_2)_7(CH_2)_2Si(OC_2H_5)_3$) and 1H,1H,2H,2H-Perfluorododecyltriethoxysilane($CF_3(CF_2)_9(CH_2)_2Si(OC_2H_5)_3$), respectively.

Figure 2-5 shows the schematic two-dimensional representations of the structures of (a) stoichiometric MoO_3 and (b) thermally-evaporated MoOx. In the stoichiometric MoO_3, six O atoms are bonded to one Mo atom. MoOx can be easily deposited in vacuum from a crucible. After the thermal evaporation, dangling bonds (O vacancies) are created in the MoOx film because of the

film preparation in an O deficient environment (in vacuum) [2].

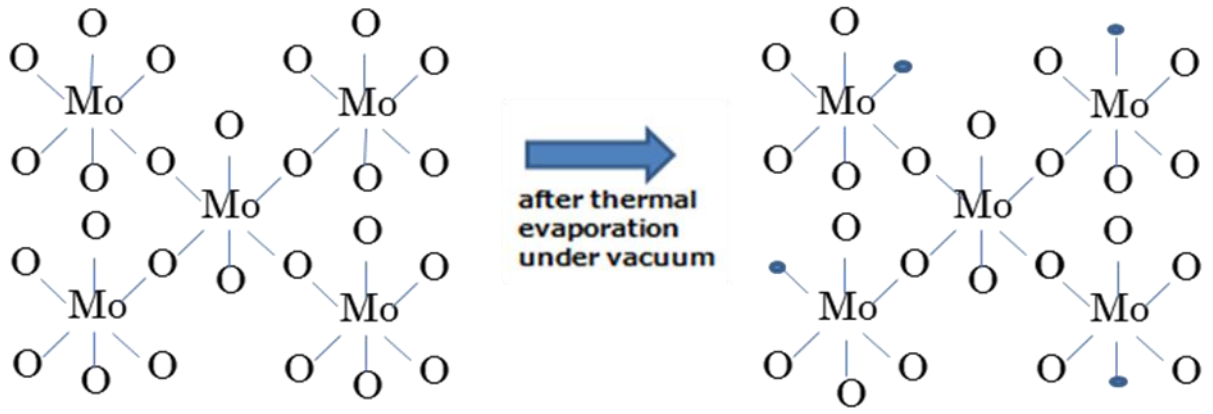

Figure 2-5 Schematic two-dimensional representations of the structures of (a) stoichiometric MoO_3 and (b) thermally-evaporated MoOx.

2-2-2 Substrate washing

In this study, ITO and glass substrates were used. ITO substrates were purchased from Geomatic and Yamanaka Hutech Co., Ltd. The substrate specifications both Geomatic and Yamanaka Hutech Co., Ltd are almost the same.The resistance and thickness of ITO are approximately 15 Ω/sq and 150 nm, respectively.

Ultrasonic cleaning processes of the glass and ITO substrates are as follows. Acetone and Semico-clean is used for removing organic materials. After the use of Semico-clean, pure water and 2-propanol are used to remove Semico-clean and moisture, respectively. Then, organic and residual organic solvents are removed by UV ozone treatments using a UV ozone cleaner (NL-UV253, Japan Laser Electronics (Present:Filgen (Co.)). Figure 2-6 shows the schematic of the UV ozone treatment equipment. After placing the substrates into the chamber, the chamber was purged by O_2 at 0.2 MPa for 45 sec. The irradiation of UV light (10 min) removed the organic materials on the substrate surface. After the UV ozone treatment, the chamber was purged by 0.2-MPa N_2 for 1 min

to eliminate the remaining ozone.

After substrate washing, the substrate is placed into the vacuum deposition chamber immediately in order to prevent contamination of the substrate surface.

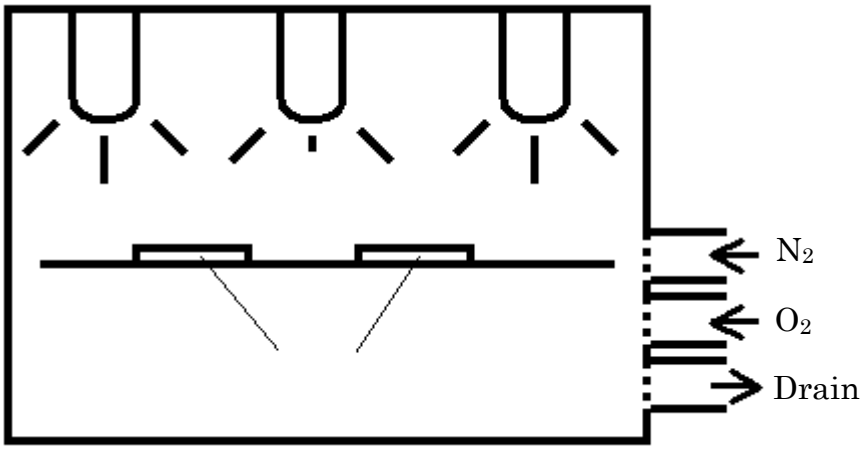

Figure 2-6 Schematic of the UV ozone treatment equipment.

2-2-3 Fabrication of organic thin films

In this study, we carried out the vacuum deposition of organic thin films, such as α-NPD and Alq3. The advantages of the vacuum deposition method used in this study are as follows.

- A vacuum deposition method is not affected by impurities, oxygen, and moisture because the deposition is carried out in a vacuum.
- Multi-layer thin filmswith different molecular materials and co-evaporation thin films are fabricated using several deposition sources.
- It is easy to control the deposition such as deposition rates.

Figure 2-7 shows the schematic diagram of the vacuum deposition system (EO-55, Eiko). The depositions of organic and inorganic materials can be implemented under the same vacuum level. The organic thin films are deposited at the left side of the vacuum deposition apparatus as shown in Fig. 2-7. Six crucibles are used as the deposition sources. The deposition rate and the film thickness are measured by a film thickness meter with a crystal oscillator. The deposition is performed under a vacuum level of the 4×10^{-4} Pa.

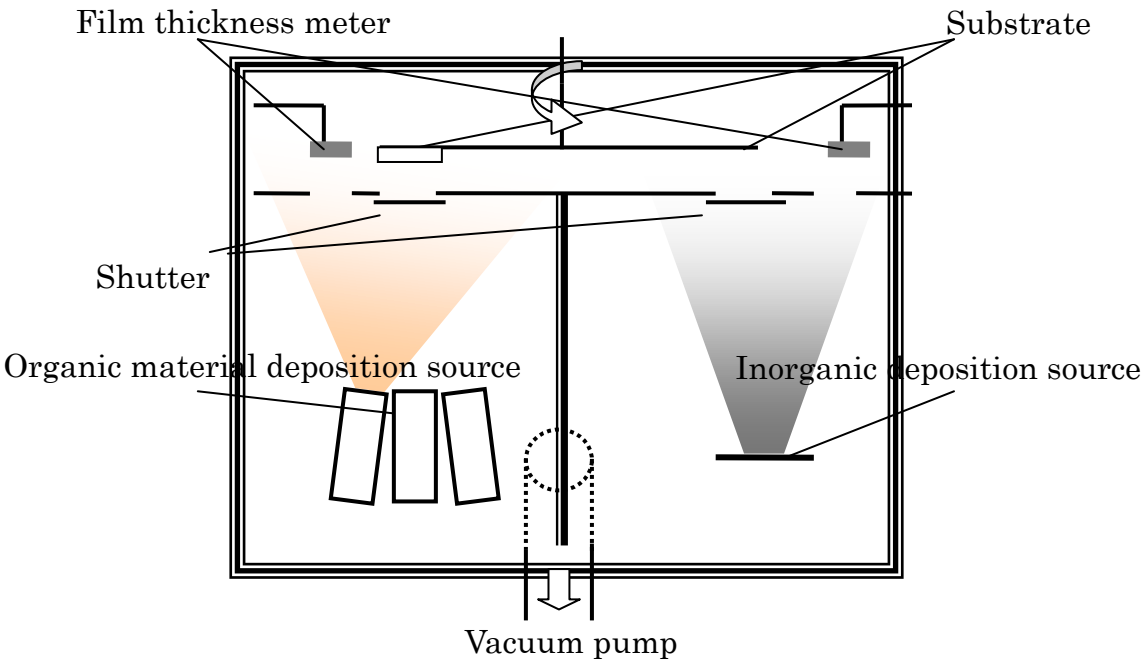

Figure 2-7 Schematic diagram of the vacuum deposition system (EO-55).

2-2-4 Fabrication of inorganic thin films

The inorganic thin films such as LiF and Al were deposited at the right side of the vacuum deposition apparatus as shown in Figure 2-7. Two tungsten boats are used as deposition sources. The deposition rate and the film thickness are measured using a film thickness meter with a crystal

oscillator. The inorganic thin film was deposited at room temperature below the vacuum level of 4×10^{-4} Pa. The area of the devices is 2 mm×2 mm = 4 mm^2.

2-2-5 Fabrication of co-evaporation thin films

Co-evaporation thin films were fabricated using a vacuum deposition apparatus (VTR-350M/ERH, ULVAC). The schematic diagram of it is depicted in Figure 2-8. The structure of the apparatus is similar to that of EO-55.

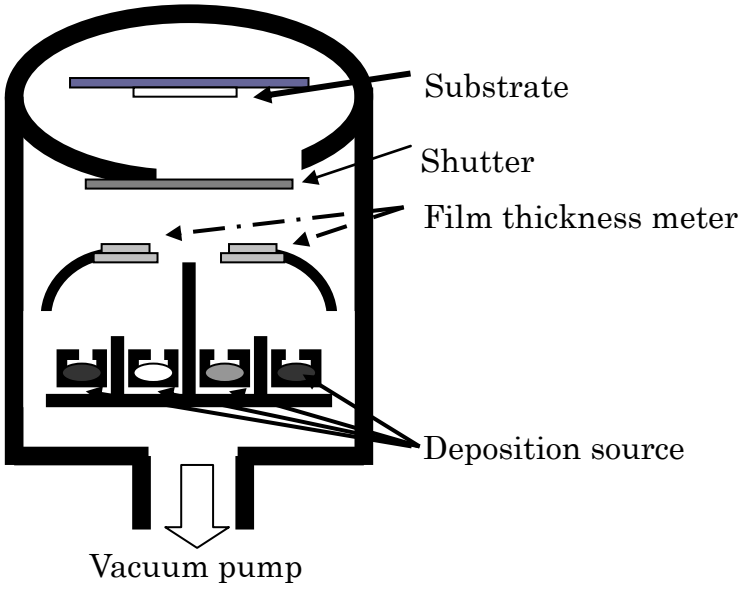

Figure 2-8 Schematic diagram of the vacuum deposition system for co-evaporation thin films (VTR-350M/ERH).

2-3 Evaluation methods

2-3-1 Contact angles

Contact angles are measured using an automatic contact angle meter (CA-VP, Kyowa Interface Science Ltd.) and an analysis software tool, FAMAS (FACE Measurement & Analysis

System). The contact angle can be automatically measured after 200 ms from dropping pure water on the substrate.

Measuring the contact angle is performed using a method as shown in Fig. 2-9. If the droplet on the substrate is assumed to be the portion of a sphere, the contact is given by

$$\theta = 2\tan^{-1}(h/a), \qquad \ldots(2.1)$$

where h is the height of the droplet and $2a$ is the apparent diameter of the droplet.

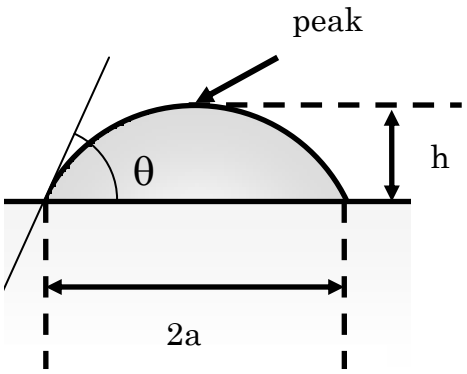

Figure 2-9 contact angle.

2-3-2 Ionization potentials and work functions

Work functions and ionization potentials are measured using a photoelectron spectroscopy (AC-3 or AC-2, Riken Keiki Co.) at room temperature. Figure 2-10 shows the configuration of the AC-2 measurement system. Monochromatic UV light is irradiated to a sample through a spectroscope and an optical fiber from a deuterium lamp, and the electrons (photoelectrons) emitted

from the sample are counted using a detector. The work function or ionization potential can be obtained from the threshold photon energy at which the photoelectron emission occurs.

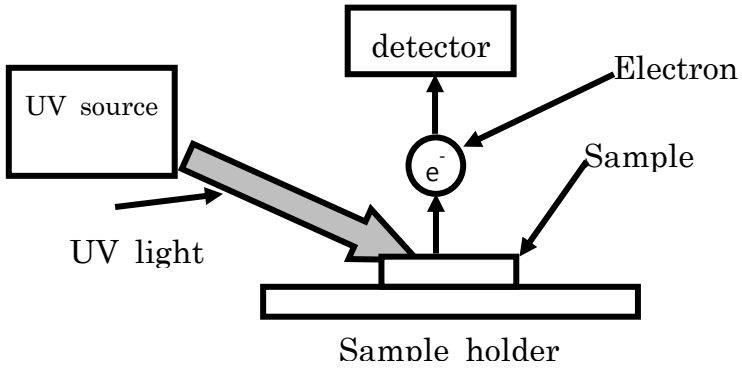

Figure 2-10 Schematic diagram of the AC-2 measurement system.

2-3-3 Dipole moment

The dipole momentswere calculated using semi-empirical molecular orbital calculation software (SCIGRESS MO Compact Version 1.0.0 Standard, Fujitsu Co.).

2-3-4 Current-Voltage-Luminance

The measurements of the current-voltage-luminance characteristic are carried out by GUI programming language (LabVIEW, National Instruments, Ltd.) under a pressure of 1×10^{-1} Pa at room temperature. The schematic of the measurement system is shown in Fig. 2-11. The luminance is measured using a luminance meter (BM-8 LUMINANCE METER, Topcon, Ltd.) and the data are collected through an RS-232C interface. The current is measured with lamp voltage (rising rate: 0.5 V/s) by a source measurement unit (2400 Source Meter, Keithley Instrument, Inc.). The currents and voltages are recorded with a personal computer through a GP-IB interface.

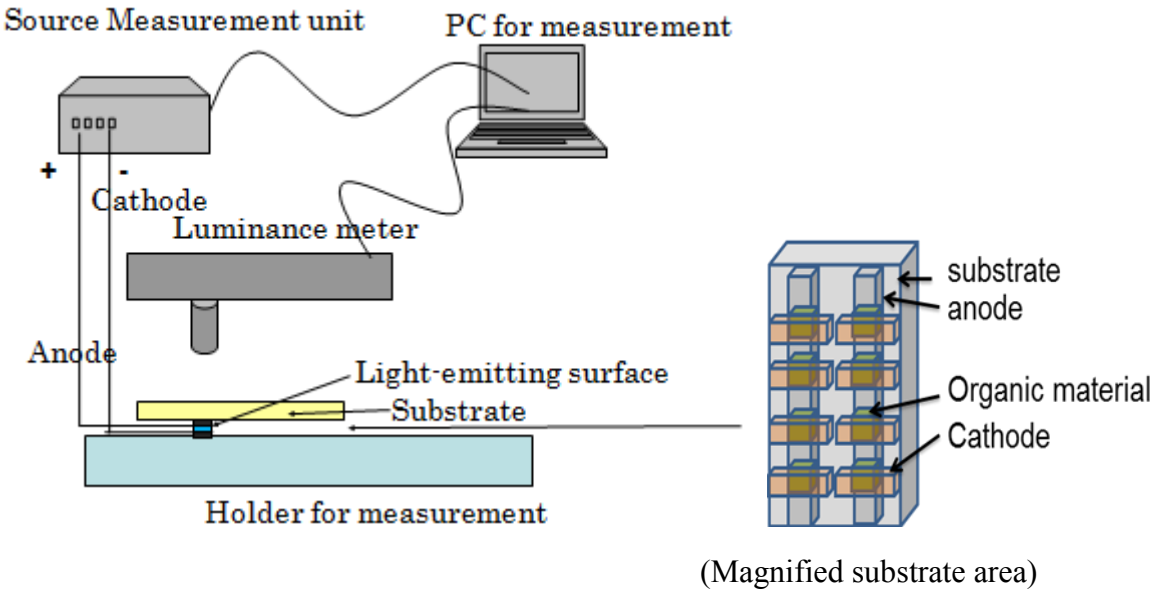

Figure 2-11 Schematic of the IVL measurement system.

2-3-5 Electroluminescent spectrum

The measurement of the Electroluminescent (EL) spectrum is carried out using a moment multi photometric system (MCPD-7000, Otsuka Electronics Co.) at room temperature.

Figure 2-12 shows the EL spectrum measurement configuration. The EL spectrum measurement system is controlled through a personal computer. The current for the device is applied using a source measurement unit (2400 Source Meter, Keithley Instruments Co.).

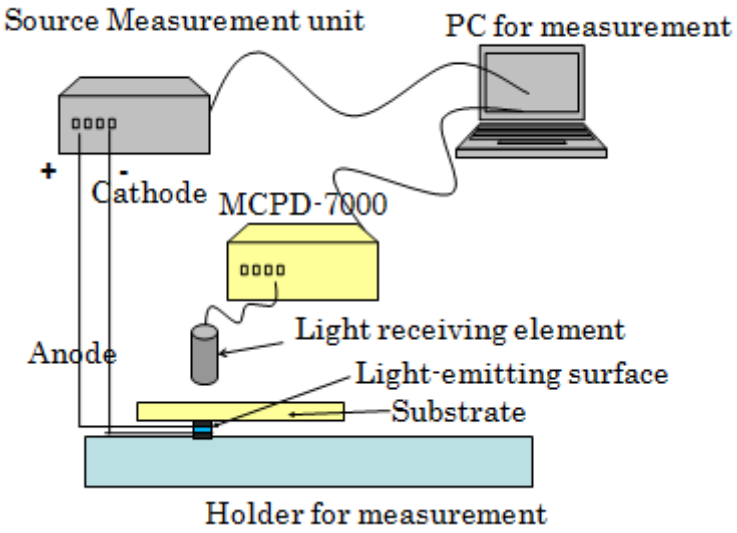

Figure 2-12 Schematic diagram of the EL spectrum measurement system.

2-3-6 Atomic force microscope

The observation of the surface status is carried out using the AFM of SPM-9600 (Shimadzu Co.).

References

[1] T. Mori, T. Morimoto, and T. Nishikawa, “Formation of Organic Nanodots on Indium Tin Oxide Using Molecular Aggregation during Self-Assembled Monolayer-Treatment Method”, Appl. Phys. Exp. 4 (2011) 111601.

[2] C.H. Cheung, W.J. Song, and S.K. So, “Role of air exposure in the improvement of injection efficiency of transition metal oxide/organic contact”, Org. Electron. 11 (2010) 89.

Chapter 3 Effects of the alkyl chain length of FSAM on OLED performance and their interface phenomena

3-1 Introduction

SAMs easily change the surface properties of substrates, because they have a dipole. The value and the direction in the dipole moment of SAMs affect the magnitude and the energy direction of the vacuum level shift, respectively [1]. The shift decreases or increases the barrier height of hole injection. Appleyard *et al.* employed SAMs at the ITO/TPD interface and reported that the work function of ITO/TPD interface with SAM increased by about 0.3 eV compared to that of bare-ITO/TPD interface [2].The turn-on voltage was reduced from 6 V of the device without SAM to 2 V. And the voltage at luminance of 300 cd/m^2 was reduced from 13.6 V to 7.88 V [2]. Manna *et al.* reported that the insertion of SAM between a cathode and an emission layer enhanced electron injection and that the turn-on voltage was about 16 V, reduced by 6 V compared to that for the device without SAM (about 22 V) [3]. Moreover, T. Mori *et al.* revealed that the FSAM-modified ITO shifted the vacuum level of HIL toward the high energy side and that it decreased the barrier height of the hole injection [4]. These indicate that the uses of SAM and FSAMs are very effective for achieving high performance of OLEDs.

The influences of SAMs with various alkyl chain lengths were investigated. Kumaki *et al.* reported organic thin-film transistors with a gate insulator treated with SAM of various alkyl chain lengths and the improvements of the on-current and the electron mobility with increasing the alkyl chain length [5]. Tao *et al.* reported that the alkyl chain length of SAMs affected the work function of the SAM-modified Ag and Au anodes and, consequently, the current density of the devices [6].

The importance of the effect of the SAM- and FSAM-modified anode on the performance of OLEDs has been recognized widely. However, full understanding on the effects of SAM and FSAM

has not been achieved. In Chapter 3, we will elucidate the effects of the alkyl chain length of FSAMs on the interface phenomena of FSAM-modified anode/HTL and the performance of OLEDs.

3-2 Properties of FSAMs with different alkyl chain lengths

3-2-1 Relationship between the dipole-moment and the alkyl chain length

Figure 3-1 shows (a) the structure of SAM and (b) FSAM molecular structure. SAM molecules consist of three elements; a bonding part, a mid section, and an end functional group. The mid-section is composed of an alkyl chain, which interacts with adjacent alkyl chains by the Van der Waals forces. Four kinds of FSAMs with different numbers of fluorine atoms were employed in this work, and were denoted by FnSAM where n is the number of C atoms and the number of F atoms is 2n–3. The direction of dipole moments in FSAM molecules is from the functional part to the bonding part.

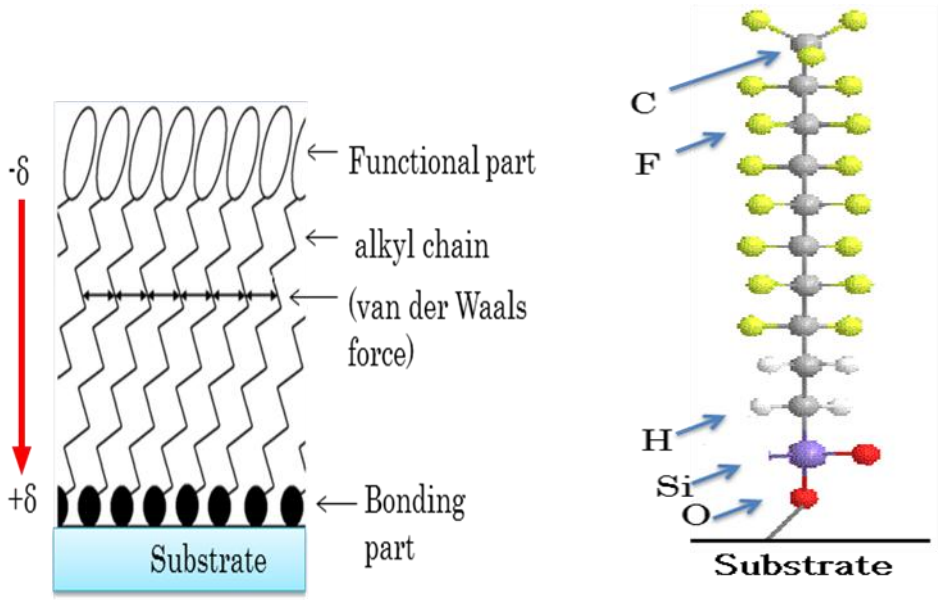

Figure 3-1 (a) structure of SAM and (b) FSAM molecular structure

The dipole moments of FSAMs were evaluated with semi-empirical molecular orbital calculation software (SCIGRESS MO. Fujitsu (Co.). Figure 3-2 shows the dipole moments of FSAMs with various alkyl chain lengths. The dipole moment is calculated by the method called Parameterized Model number 3 (PM3). PM3 model is used due to the expediency of molecular orbital calculations with several atoms (C, F, H and Si) utilizing experiment. The dipole moments of FSAM molecules originate from the strong electronegativity difference between F (electronegativity: 4) and C atoms (electronegativity: 2.5). With the increase in alkyl chain lengths, the dipole moments increase slightly. However, the dipole moments of F8SAM, F10SAM and F12SAM were almost the same. The upper parts in FSAM molecules between the F8SAM and the F12SAM are almost the same due to the tight-binding state as same molecular structures (CF_3) of the fluorocarbon. The perpendicular dipole moments of the top CF_3 group to the FSAM molecular axis are generated since the C-F dipole moments of the middle side alkyl chain are canceled mutually. Therefore, the dipole moments in F8SAM, F10SAM, and F12SAM are almost same owing to the same molecule structures of the fluorocarbon of the upper parts in FSAM molecules and the mutual cancelations of middle side alkyl chains.

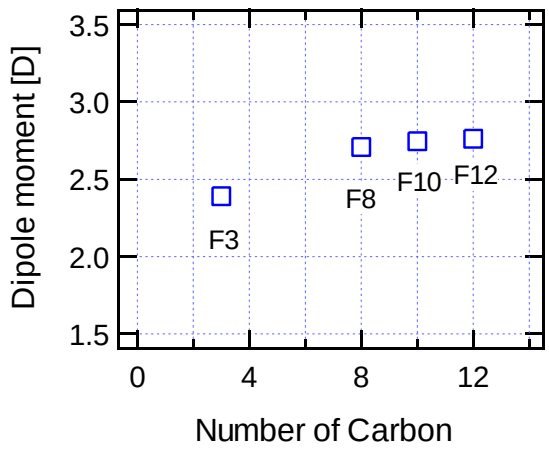

Figure 3-2 Dipole moments of FSAMS with various alkyl chain lengths.

3-2-2 Relationship between the work-function and the alkyl chain length

The magnitude of dipole moments affects work functions. Figure 3-3 shows the work function of the FSAM-modified ITO with various alkyl chain lengths. When the F12SAM is compared with the F8SAM, the F12SAM has 6 more fluorine atoms than the F8SAM. The C-F dipole moment is 1.6 D. When the direction of C-F dipole moments is in a similar direction, the FSAM molecule may have a larger dipole moment. However, even if the fluorinated alkyl chain becomes longer, the dipole moment of FnSAM molecule do not increase remarkably. Because the C-F dipole moments in the chain are cancelled by each other and the three C-F dipole moment of the end (top) contributes to the dipole moment of FnSAM molecule.

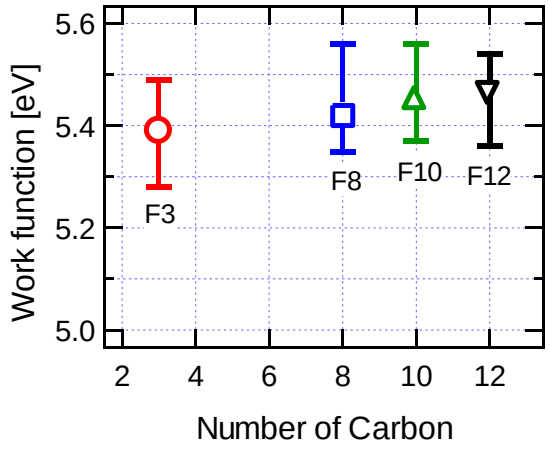

Figure 3-3 Work functions of the FSAM-modified ITO with various alkyl chain lengths.

3-2-3 Relationship between the contact-angle and the alkyl chain length

Forming FSAM on the ITO substrates was investigated with contact angles of water droplets. Figure 3-4 shows the droplets on the bare ITO substrate and on FSAM-modified ITO substrates. Figure 3-5 shows the contact angle of the FSAM-modified ITO with various alkyl chain lengths. As

the alkyl chain length increased, the contact angle increased, indicating that the surface of the FSAM-modified ITO was more hydrophobic. However, the differences in the contact angles among F8SAM, F10SAM and F12SAM were small.

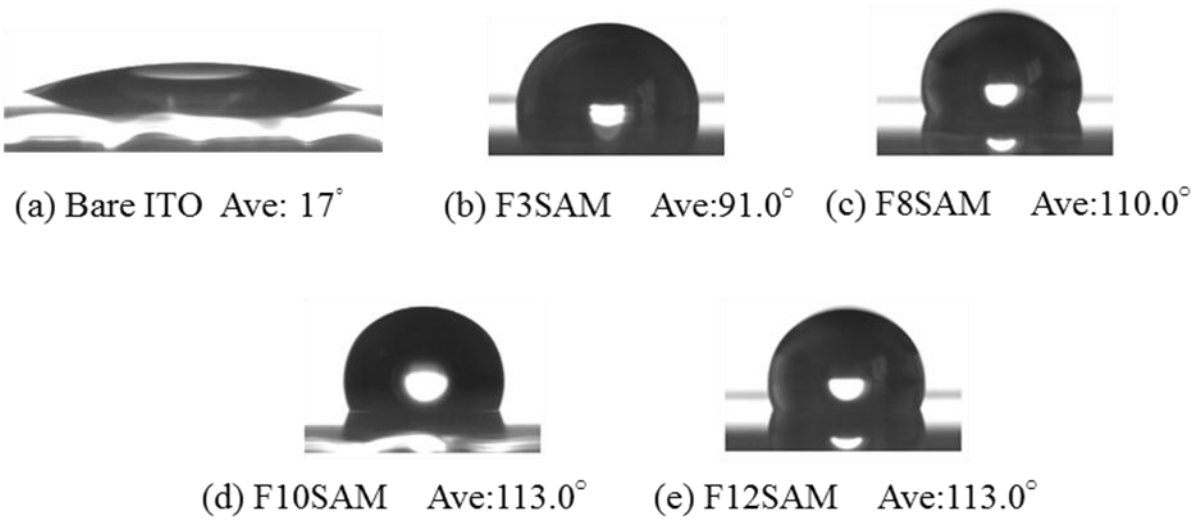

Figure 3-4 Droplets on the bare ITO and the FSAM-modified ITO.

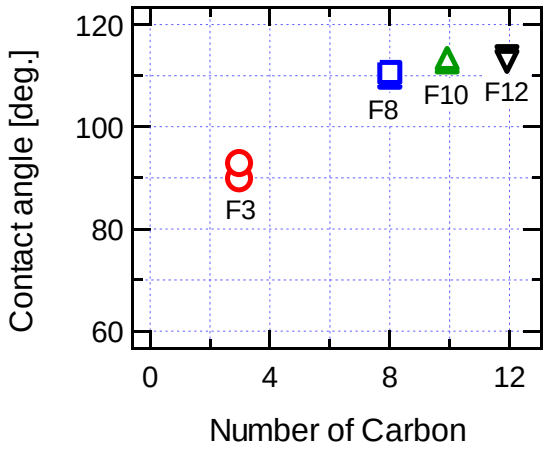

Figure 3-5 Contact angles of water droplets on FSAM-modified ITO.

The coverage ratio, C_1 ($0 \le C_1 \le 1$), was calculated, based on the Cassie's law. It is given by the following equation,

$$\cos\theta = (1 - C_1)\cos\theta_1 + C_1 \cos\theta_2, \quad \ldots(3.1)$$

where θ is the contact angle for FSAM-modified ITO, θ_1 is the contact angle for bare ITO and is the contact angle for FSAM. In this work, the contact angle of the bare ITO was estimated to be 17^o and the contact angle of FSAM was 113^o on the assumption that F12SAM could cover ITO completely. The values calculated from the eq. (3-1) are shown in Table 3-1. With the increase in the alkyl chain length, the FSAM molecules covered the ITO substrate surface more completely. This is caused by the enhancement of molecular alignment of the strong interchain interactions (van der Waals forces) with longer alkyl chain lengths. Figure 3-6 shows the schematic diagrams of F3SAM and F12SAM molecule alignments. Because of the short alkyl chain of F3SAM, the van der Waals force between the alkyl chains is weak and the alignment of the F3SAM molecules is not perfect, leading to the partially-uncovered ITO surface. In contrast, as the F12SAM molecules have a longer alkyl chain, the alignment of the F12SAM molecules became more perfect and the ITO surface was covered completely with the F12SAM molecules. It is noted that F8SAM molecules covered the ITO surface with high coverage ratio, as shown in Table 3-1.

Table 3-1 Coverage ratios of FSAMs on the ITO substrate

Material	Contact angle [°]	Coverage ratio [%]
F3SAM	91	72
F8SAM	110	95
F10SAM	113	100
F12SAM	113	100

(The coverage ratio of F12SAM is assumed to be 100%)

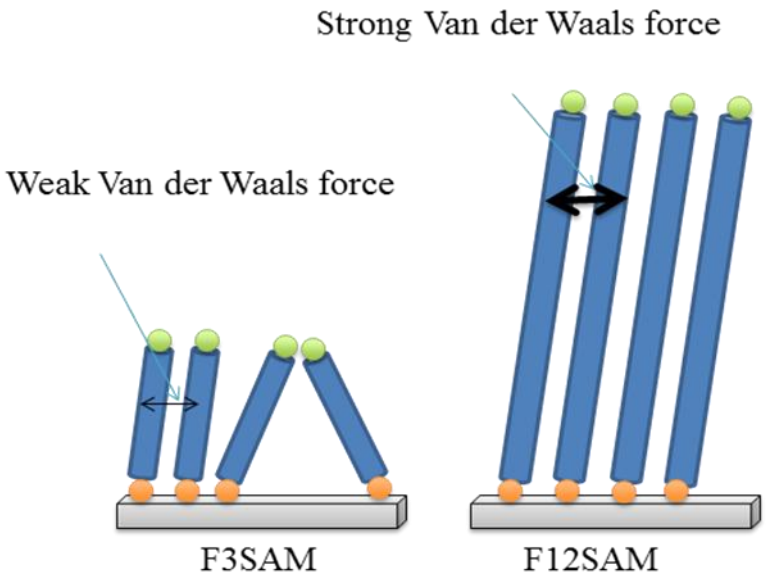

(a) F3SAM (b) F12SAM

Figure 3-6 Schematic diagrams of the alignments of F3SAM and F12SAM

3-3 Investigation of the electrical characteristics of FSAMs with different alkyl chain lengths

Figure 3-7 shows the current density-voltage characteristics of the ITO/FSAM/α-NPD (50nm)/Alq3(50nm)/LiF(0.6nm)/Al devices with various FSAMs. The threshold voltages of all devices were about 2 V. The same threshold voltages is due to the slight difference in the hole

injection barriers of various FSAMs. It has been considered that the increase in the alkyl chain length enhances a disturbance of the carrier transport because of the insulating alkyl chain. However, the current of the device with longer alkyl chain was higher at the same applied voltages.

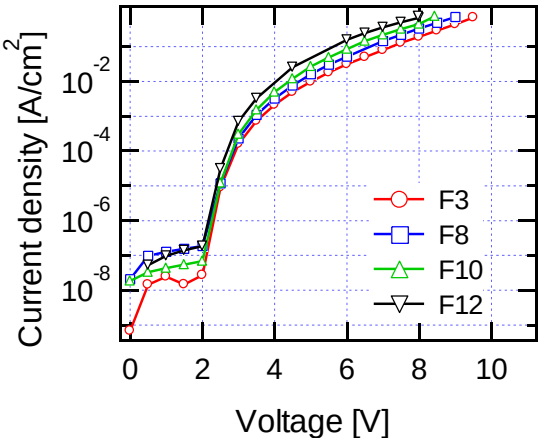

Figure 3-7 Current density–voltage characteristics of the ITO/FSAM/α-NPD(50nm)/Alq3 (50nm)/LiF (0.6nm)/Al.

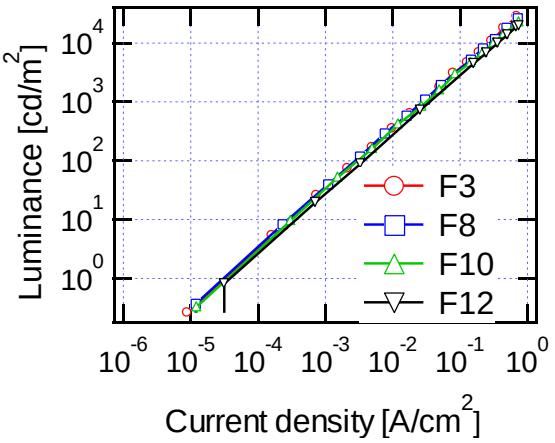

Figure 3-8 Luminance-current density characteristics of the ITO/FSAM/α-NPD (50nm)/Alq3(50nm)/LiF(0.6nm)/Al.

Figure 3-8 shows the luminance-current density characteristics the ITO/FSAM/ α-NPD(50nm)/Alq3(50nm)/LiF(0.6nm)/Al devices with various FSAMs. The devices with FSAM-modified ITO showed the same luminance per current density. The barrier height of the hole injection for the devices with FSAM-modified ITO is decreased, and the hole injection is enhanced. The carrier balance can be broken when only hole current increases unilaterally, leading to a degradation of EL efficiency. However, the EL efficiencies of the luminance per current density were not varied with the alkyl chain length of FSAM. The cause of this seems a sufficient electron injection from the LiF/Al cathode to the Alq3 layer, and the carrier balance was kept even if the hole injection was enhanced. This indicates that further improvement of the hole injection can lead to high performance of OLEDs.

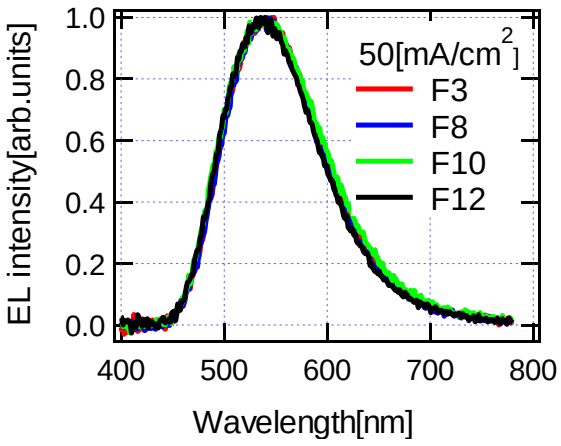

Figure 3-9 EL spectra of the ITO/FSAM/α-NPD(50nm)/ Alq3(50nm)/LiF(0.6nm)/Al devices at 50 mA/cm^2.

Figure 3-9 shows the EL spectra of the devices with various FSAMs. Regardless of the alkyl chain lengths, the EL spectra showed the same peak wavelength (about 540nm) and the same width as those from Alq3. These indicate that the recombination region is not affected by FSAM.

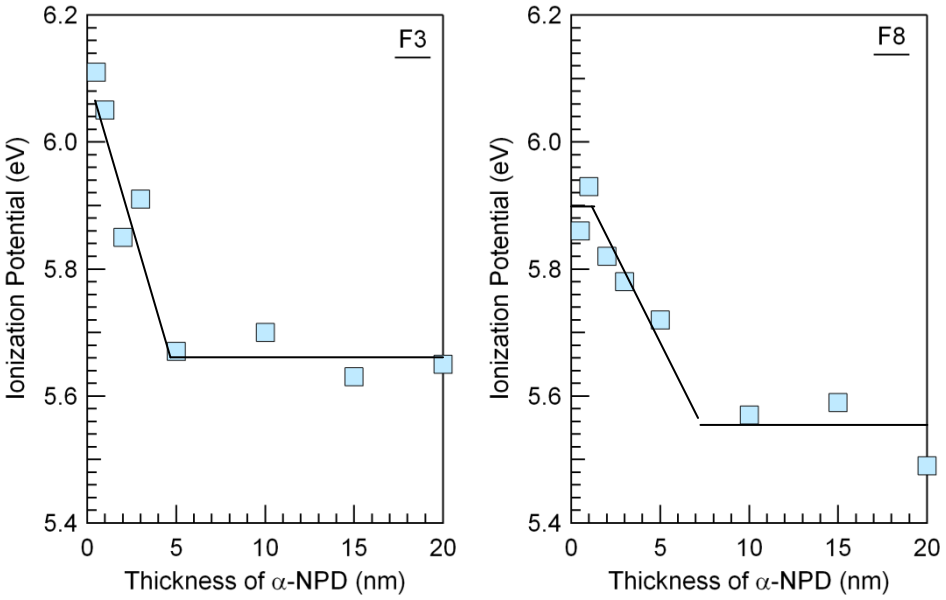

(a) F3SAM (b) F8SAM

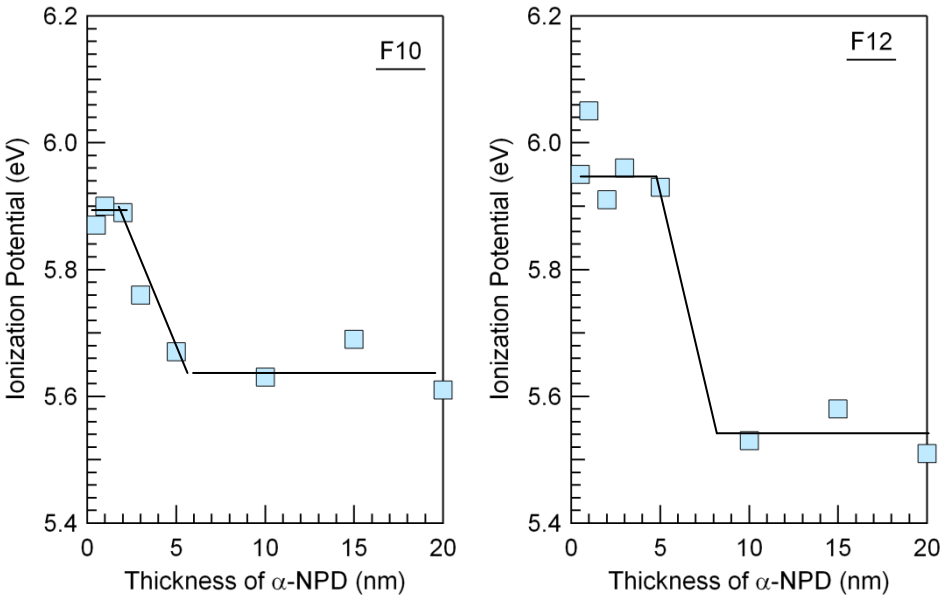

(c) F10SAM (d) F12SAM

Figure 3-10 Dependences of the ionization potentials of the FSAM-modified ITO on the thickness of α-NPD layer.

The current of the device with longer alkyl chain was higher although the alkyl chain is an insulator. This can be explained as follows. Satoh *et al.* investigated the phenomena of the interface between FSAMs with various alkyl chain lengths and α-NPD of HTL using UPS [7]. Figure 3-10 shows the dependences of the ionization potentials of the FSAM-modified ITO, estimated by Satoh *et al*., on the thickness of α-NPD layer. As the thickness of α-NPD layer increased, the ionization potentials reduced and reached the value of α-NPD at respective thicknesses. As shown in Fig. 3-10, the regions where the ionization potential was constant with the thickness of α-NPD layer were formed on the FSAM/α-NPD interfaces (we called it "transition region"). As the alkyl chain length of FSAM increased, the transition region widened. Inden et al. applied the impedance method to the FSAM-modified ITO/α-NPD devices and revealed the formation of high conductive regions in α-NPD layer on FSAMs [8]. That is, the transition region is highly conductive and enhances the higher current even when FSAM with longer alkyl chain is employed in the device.

3-4 Summary

In this chapter, we discussed the EL properties of OLEDs with FSAMs of various alkyl chain lengths as HIL. It was originally thought that hole injection was enhanced because of the increase in the dipole moment of FSAM molecules with increasing the number of F atoms. However, the work function of FSAM-modified ITO was scarcely affected by the alkyl chain length. The cause is that the dipoles with the F atoms of the alkyl chain are canceled and the dipoles of the FSAM molecules are dominated by that of $–CF_3$ at the end of the alkyl chain.

The current of the device with FSAM of the longer alkyl chain was higher. It has been considered that longer alkyl chain prevent the carrier transport because it is an insulator. However, UPS and the impedance method revealed the highly-conductive transition region was formed on FSAM/α-NPD interface. The conductive region induced the high carrier transport in the device with

FSAM of the longer alkyl chain.

FSAMs are available commercially only if the number of F atoms is below eight. In this work, however, it has been found that the OLEDs with F8SAM have the sufficient performance although the use of FSAM with longer alkyl chain achieves higher performance of OLEDs. This is important in practically applying FSAMs to OLEDs.

References

[1] C. Ganzorig, K. J. Kwak, K. Yagi, and M. Fujihira, "Fine tuning work function of indium tin oxide by surface molecular design: Enhanced hole injection in organic electroluminescent devices", Appl. Phys. Lett. 79 (2) (2001) 272.

[2] S. F. J. Appleyard, S. R. Day, R. D. Pickford, and M. R. Willis, "Organic electroluminescent devices: enhanced carrier injection using SAM derivatized ITO electrodes", J. Mater. Chem. 10 (2000) 169.

[3] U. Manna, H.M. Kim, M. Gowtham, J. Yi, S. Sohn, D. Jung, "Enhanced carrier injection of organic light emitting devices using self assembled monolayer in the cathode/organic interface", Thin Solid Films. **495** (2006) 380.

[4] T. Mori, M. Imanishi, and T. Nishikawa, "Electrical Conduction Behavior of Organic Light-Emitting Diodes Using Inhomogeneous Fluorinated Self-Assembled Monolayer as a Hole-Injection Layer", Appl. Phys. Exp. 4 (2011) 071601.

[5] D. Kumaki, S. Ando, S. Shimono, Y. Yamashita, T. Umeda and S. Tokito, "Significant improvement of electron mobility in organic thin-film transistors based on thiazolothiazole derivative by employing self-assembled monolayer",Appl. Phys. Lett.**90** (2007) 053506.

[6] Y. Tao, K. Wub, K. Huang, and T. Perng, "Odd–even modulation of electrode work function

with self-assembled layer: Interplay of energy barrier and tunneling distance on charge injection in organic light-emitting diodes", Org. Electron. **12** (2011) 602.

[7] T. Satoh, M. Imanishi, T. Nishikawa, and T. Mori, "Properties of Interface between Organic Hole-Transporting Layer and Indium Tin Oxide Anode Modified by Fluorinated Self-Assembled Monolayer", Jpn. J. Appl. Phys. **51** (2012) 035701.

[8] T. Inden, M. Imanishi, T. Nihsikawa, and T. Mori, "Interface Phenomena between Diamine Derivative and Fluorinated Self-Assembled Monolayer", 9th International Conference on Electroluminescence and Organic Optoelectronics, Fukuoka, Japan, Sept. 3-7 (2012) P-94.

Chapter 4 Investigations of the co-evaporation thin film of MoOx and the α-Naphthyl Diamine Derivative in OLEDs

4-1 Introduction

MoOx is used as HIL as described in the section 1-3-2. In 1996, Tokito et al. introduced MoOx as HIL in OLEDs. Driving voltages of the device using MoOx as HIL are decreased due to the low barrier height of hole injection at a metal oxide/TPD interface (They defined an driving voltage for current injection of 10 mA/cm^2) [1]. Also, it is reported that the MoOx can be used to improve the voltage as HIL. The device with MoOx can reduce the voltage under constant currents compared to that without MoOx. Voltages for OLEDs with and without MoOx substrates at 10 mA/cm^2 are 6.8 and 8.8 V, respectively. The voltage of the device with MoOx at 10 mA/cm^2 is remarkably decreased. In this paper, the driving voltage is defined as the voltage for current density at approximately 10 A/cm^2 [2].

In various hole transport materials, α-NPD is one of the most commonly used materials as HTL. α-NPD is a hole conductor with two triarylamine groups and applied to OLEDs because of its (α-NPD) adequate hole mobility of about 10^{-4} cm^2/Vs [3]. Tokito *et al.* introduced the MgF_2 doped N,N'-diphenyl-N, N'-bis(3-methylphenyl)-[1,1'-biphenyl]-4,4'-diamine (TPD) as HTL in OLEDs [4]. In OLEDs with the MgF_2 containing TPD, the threshold voltage of light emission is estimated to be 6 V and a high luminanceof 2600 cd/m^2 is achieved at a current density of 240 mA/cm^2 with the voltage of 15 V. This is first suggestion to use an organic-inorganic hybrid system to improve OLED performance.

Kröger *et al.* investigated influences of p-type doping in organic wide band gap materials by using MoOx. MoOx is co-evaporated with organic materials, α-NPD and 4,4'-Bis(N-carbazolyl)-1,1'-biphenyl (CBP). The Fermi level of co-evaporation thin films is shifted

towards the HOMO level of co-evaporation thin films by MoOx doping. Moreover, the work function of the co-evaporation thin film is also increased [5]. Matushima *et al.* reported the evidence of the charge transfer phenomena between MoOx and organic materials. By comparing the current density-voltage characteristics, the organic material-to-MoOx electron transfer is crucial to realize SCLC. They confirmed the charge transfer phenomena from the observation of the SCLC using the MoOx layer [6].

It is reported that co-evaporation thin film of MoOx:α-NPD in OLEDs improves performance [5,6]. The purpose of our research is improvement analysis of the charge carrier injection and transport in the co-evaporation thin film of MoOx:α-NPD in OLEDs. (The co-evaporation thin films often show degraded OLED performance due to poor electrical properties such as carrier mobility and density). We investigate the film properties of co-evaporation thin films of MoOx and α-NPD. We also investigate their electrical characteristics.

4-2 Film properties of co-evaporation thin films of α-NPD and MoOx as a hole injection layer

4-2-1 Work function of co-evaporation thin films of α-NPD and MoOx

Both Ag and ITO are used as anode materials. The Ag anode is tried as an alternative electrode to indium tin oxide (ITO) due to the limited supply and brittleness of indium. Therefore, we used the Ag anode and compared the results with those with an ITO anode.

The co-evaporation thin films are deposited with the ratio of α-NPD:MoOx=1:1 simultaneously. Figure 4-1 shows the work functions of various HILs measured by using a photoemission yield spectroscopy in air. The work functions of ITO, Ag(20nm), Ag(20nm)/MoO_x(10nm), ITO/MoO_x(10nm), Ag(20nm)/MoO_x:α-NPD(1:1,10nm), ITO/MoO_x: α-NPD(1:1,10nm), and α-NPD are estimated to be 5.0, 4.7, 5.73, 5.70, 5.34, 5.36, 5.45, and 5.4 eV, respectively. The work function of the MoOx layer is higher than those of ITO and the Ag anode by

more than 0.7 eV. Although there is no barrier height between MoOx and α-NPD, the injection efficiency is thought to be poor because work function is too deep. The work function of a co-evaporation thin film is higher than those of ITO and Ag anode by more than 0.34 eV. The work function of the FSAM-modifed ITO is 0.45 eV higher than that of ITO. There is almost no barrier height between hole injection material-modified anode and α-NPD. Therefore, the carrier injection from hole injection material is higher than that from the anode. It is suggested that the energy matching between MoOx and α-NPD can be improved by the co-evaporation.

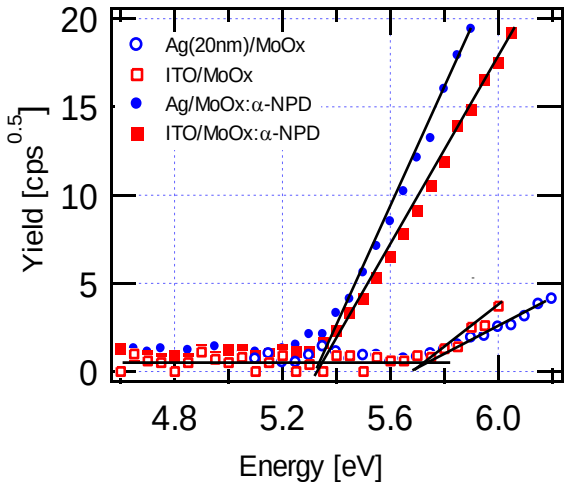

Figure 4-1 Square root of the photoemission yield-energy spectra.

Table 4-1 Work functions with different substrate structures

Device	Work function [eV]
ITO	5.0
Ag	4.7
ITO/MoOx	5.73
ITO/MoOx: α-NPD	5.36
Ag/MoOx	5.70
Ag/MoOx: α-NPD	5.34
ITO/FSAM	5.45

4-2-2 Transmittances of co-evaporation thin films of α-NPD and MoOx

Transmittances of substrates with anode and hole injection materials are shown in Fig.4-2. The transmittance of an 150nm-thick ITO anode is over 75% in visible light range. Since a thick Ag film is opaque, we deposit a 20nm-thick thin-film in order to extract light. It is reported that the grain size of the Ag film deposited on substrate is fairly large due to the agglomeration of Ag atoms [7]. The grain size of Ag thin film deposited on substrate is large up to approximately the 10nm of Ag. However, the morphology of the Ag film changed smoothly with increasing Ag film thickness. It is considered that the optimal thickness for extracting light with the opaque characteristics in a Ag film represents a thickness of about 20nm. Therefore, the transmittance of the 20nm-thick Ag is lower than that of the ITO substrate. We use the low transmittance characteristics of 20nm-thick Ag. The transmittance of the ITO substrates with a co-evaporation thin film is lower than that with MoOx layers.

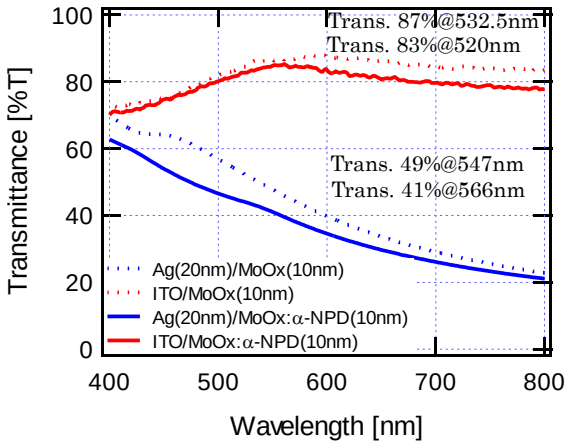

Figure 4-2 Transmittance of the co-evaporation thin film or MoOx layer.

4-2-3 AFM observation of co-evaporation thin films of α-NPD and MoOx

Figure 4-3 shows AFM images of the co-evaporation thin film- or MoOx-deposited substrates. The Maximum peak heights (Rp) of Ag/MoOx, Ag/MoOx: α-NPD, ITO/MoOx, and ITO/MoOx:α-NPD are estimated to be approximately 17.5, 15.4, 18.1, and 15.0 nm, respectively. The Maximum valley depths (Rv) of Ag/MoOx, Ag/MoOx: α-NPD, ITO/MoOx, and ITO/MoOx: α-NPD are estimated to be approximately -10.8, -11.0, -11.8, and -12.6 nm, respectively. The average roughness is described as follows

$$R_a = \frac{1}{L}\int_0^L |Z(x)|\,dx, \qquad \ldots (4.1)$$

where $Z(x)$ is the function that describes the surface profile analyzed in terms of height Z and position (x) of the sample over the evaluation length L. Thus, the R_a is the arithmetic mean of the absolute values of the height of the surface profile $Z(x)$.The calculated average roughnesses (R_a) of Ag/MoOx, Ag/MoOx:α-NPD, ITO/MoOx,and ITO/MoOx:α-NPD are estimated to be

approximately 2.57, 2.27, 1.81, and 2.18 nm, respectively. The shape of the surface roughnesses in Ag/MoOx, Ag/MoOx:α-NPD,andITO/MoOx:α-NPD is similar to each other. The roughness shapes in peaks and valleys from the Fig. 4-4 are indicated. Therefore, the hole injection from modified ITO substrates is not affected by the surface roughness, that is, a strong localized electric filed.

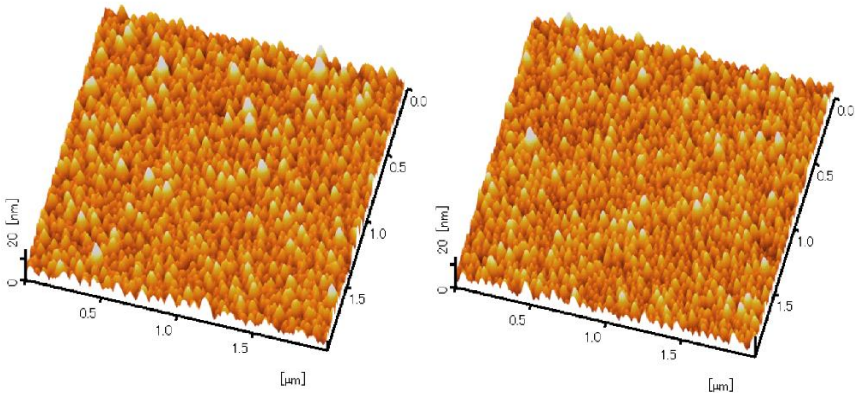

(a) Ag/MoOx 3D (b)Ag/MoOx:α-NPD 3D

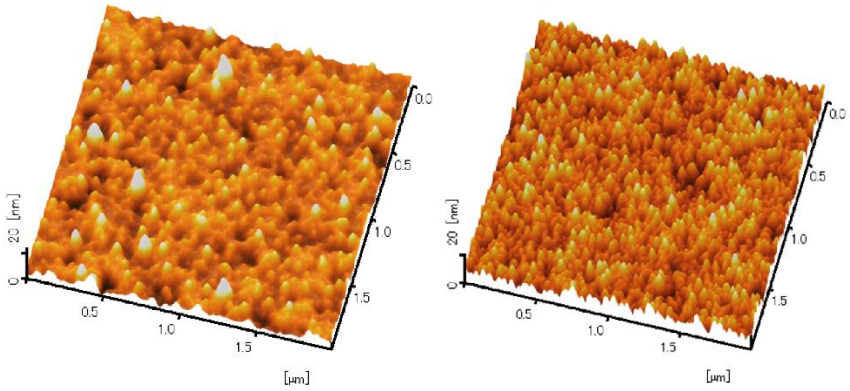

(c) ITO/MoOx 3D (d) ITO /MoOx:α-NPD 3D

Figure 4-3 AFM images of HIL on the anode (a) AFM image of the MoOx layer on a Ag anode (b) AFM image of the MoOx layer on an ITO anode (c) AFM image of the co-evaporation thin film of MoOx:α-NPD on a Ag anode (d) AFM image of the co-evaporation thin film of MoOx:α-NPD on an ITO anode.

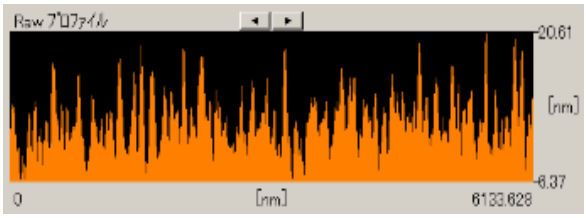

(a) Ag/MoOx raw profile

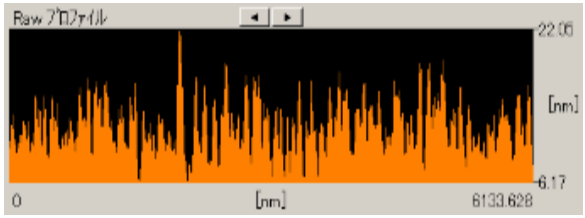

(b) Ag/MoOx:α-NPD raw profile

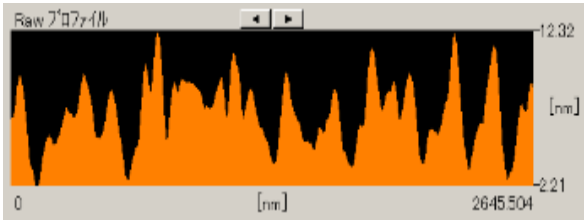

(c) ITO/MoOx raw profile

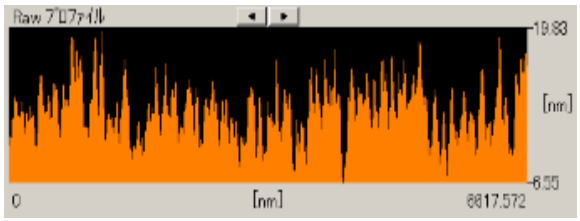

(d) ITO/MoOx:α-NPD raw profile

Figure 4-4 AFM raw profile of HIL on the anode (a) AFM image of a MoOx layer on the Ag anode (b) AFM image of a co-evaporation thin film of MoOx:α-NPD on the Ag anode(c) AFM image of a MoOx layer on the ITO anode (d) AFM image of a co-evaporation thin film of MoOx:α-NPD on the ITO anode.

Table 4-2 Substrate roughness of HIL on the anode

Substrate structure	Ra [nm]	Rp [nm]	Rv [nm]
Ag/MoOx	2.57	17.5	-10.8
Ag/MoOx:α-NPD	2.27	15.4	-11.0
ITO/MoOx	1.81	18.1	-11.8
ITO/MoOx:α-NPD	2.18	15.0	-12.6

4-3 Electrical conduction mechanism of co-evaporation thin films

We investigated the electrical conduction mechanism of both the co-evaporation thin film and the α-NPD thin film. Figure 4-5 shows the current density–voltage characteristics of the devices with co-evaporation thin films or α-NPD thin films. First I tried to measure the current–voltage characteristics of co-evaporation thin film. The first structure of the device is ITO/MoOx:α-NPD (1:1,50nm or 100nm)/Al(100nm). The device with a co-evaporation thin film causes an electrical short circuiting problem even if the thickness is 100 nm-thick. Therefore, FSAM is inserted between ITO and a co-evaporation thin film. FSAM prevents an electrical short between both electrodes. In addition, the use of FSAM-modified ITO can lead to almost Ohmic-like contact, that is, a smooth hole injection from ITO to α-NPD. The structure of the devices with a co-evaporation thin film was modified as ITO/FSAM/α-NPD(50nm or 100nm) or MoOx:α-NPD(1:1,50nm or 100nm)/Al(100nm). The current densities of co-evaporation thin film are much higher than those of α-NPD thin film.

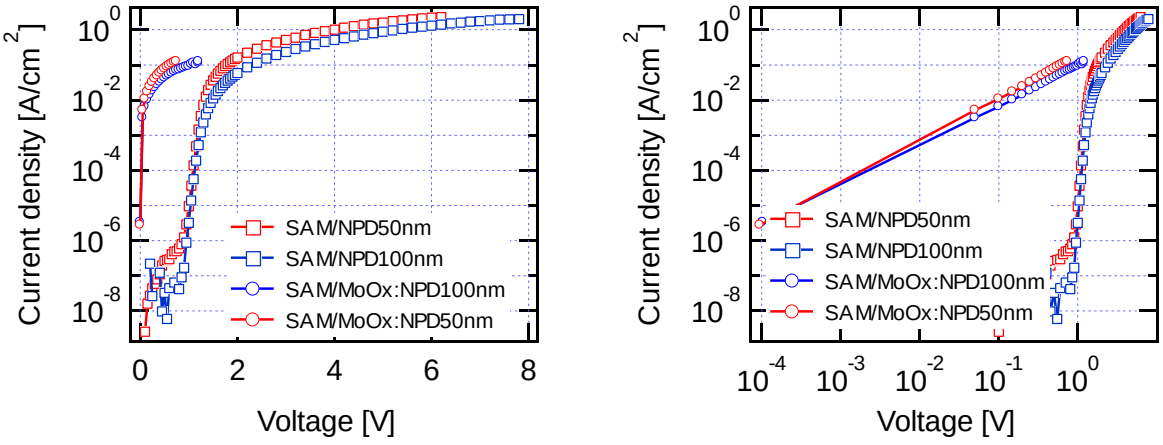

(a) Log-linear scale (b) log-log scale

Figure 4-5 Current density–voltage characteristics of the devices with a co-evaporation thin film or an α-NPD thin film where the device structure is ITO/MoO_x:α-NPD(1:1,50nm or 100nm) or α-NPD (50nm or 100nm) /Al(100nm). log-linear scale (a) log-log scale (b)

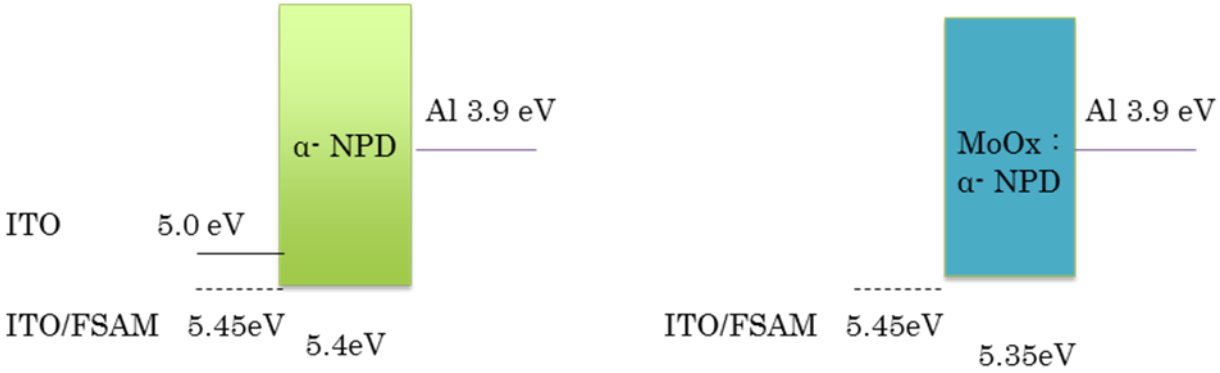

(a) α-NPD thin film (b) co-evaporation thin film

Figure 4-6 Energy diagram of the device with a α-NPD thin film (a) a co-evaporation thin film (b).

Figure 4-6 shows the energy diagram of a co-evaporation thin film or an α-NPD thin film. The work function of the FSAM-modified ITO is increased from 4.9～5.0 eV to 5.45 eV. The ionization potentials of co-evaporation thin film and α-NPD are estimated to be 5.35 eV and 5.4 eV [5], respectively. The barrier height of hole injection between ITO and HTL (α-NPD or

co-evaporation thin film) is decreased. Figure 4-7 shows the plot of current density vs. squared voltage (J-V^2) for FSAM/α-NPD specimens. When a bare ITO is used as an anode, the J-V^2 curve is not always linear. However, when the FSAM-modified ITO is used, the J-V^2 curve shows the linear behavior.

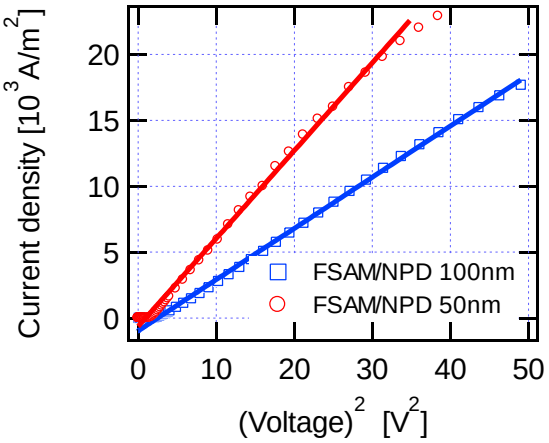

Figure 4-7 Current density-square of voltage characteristics in ITO/FSAM/α-NPD (50nm or 100nm)/Al(100nm) where symbols and lines represent experimental results and fitting data respectively.

Table 4-3 Slope used for the curve fitting in Fig.4-7

Device structure	Slope [A / (V m)^2]
FSAM/ α-NPD(50nm)	620.41
FSAM/ α-NPD(100nm)	350.677

The mobility of an α-NPD thin film can be calculated by the SCLC model. If the current density characteristic satisfies the space charge limited current (SCLC) theory, the slope in the current density-square of voltage characteristicsis given by $\frac{9}{8}\frac{\mu\varepsilon}{d^3}$ ($\because J=\frac{9}{8}\varepsilon_0\varepsilon_r\mu\frac{V^2}{d^3}$). The slopes

with FSAM/α-NPD(100nm) and with FSAM/α-NPD(50nm) are estimated to be approximately 350.677 and 620.41[A / (V m)^2], respectively.

$$J = \frac{9}{8}\varepsilon\mu\frac{V^2}{d^3}, \quad \ldots (4.2)$$

$$Slope = \frac{9}{8}\frac{\mu\varepsilon}{d^3}, \quad \ldots (4.3)$$

$$\mu = Slope \times \frac{8}{9}\frac{d^3}{\varepsilon}, \quad \ldots (4.4)$$

When the carrier mobility of α-NPD can be calculated as the dielectric constant of α-NPD is assumed to be 3, the hole mobilities of α-NPD thin films are estimated to be 2.60 x 10^{-9} m^2/Vs(50 nm) and 1.17 x 10^{-8} m^2/Vs(100 nm) from the equation (4.4). The α-NPD mobility obtained from the time-of-flight method is reported to be ~ 4 x $10^{-8}$$m^2$/Vs [8,9]. Our results are the same as or lower than the hole mobility obtained from the time-of-flight method. On the other hand, the carrier mobility of co-evaporation thin films is predicted to be much larger than the hole mobility of α-NPD since the currents of co-evaporation thin films show no behavior of SCLC. However, the current densities of co-evaporation thin films are almost ohmic against the voltage but show a threshold voltage before the ohmic behavior as shown in Fig. 4-8.

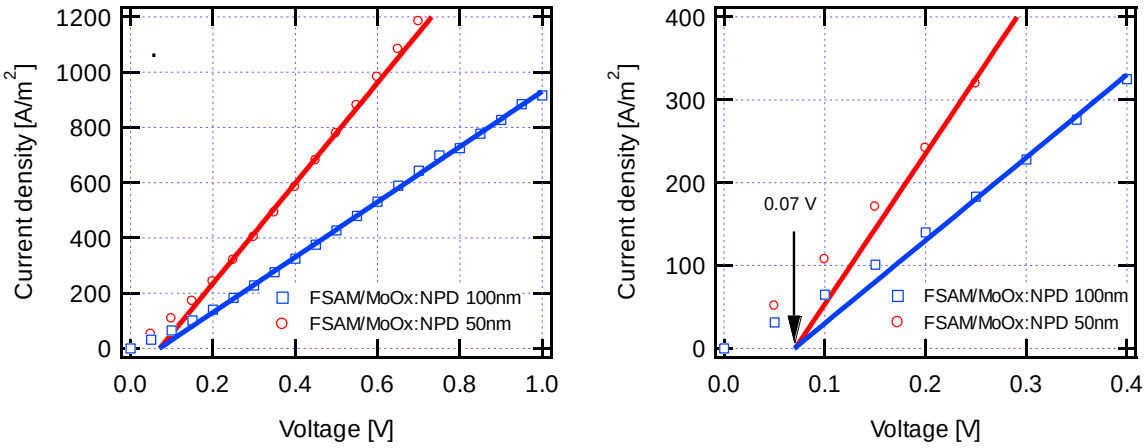

(a) J-V characteristics (b) Enlarged low voltage region of J-V characteristics

Figure 4-8 Current density-voltage characteristics of ITO/FSAM/MoO_x:α-NPD (50nm or 100nm)/Al(100nm) (a): enlarged low voltage region (b) where symbols and lines represent experimental results and fitting data respectively.

Figure 4-8 shows the current density-voltage characteristics in co-evaporation thin films as fitting data results with Fig. 4-7. The current density of the co-evaporation thin film shows an Ohmic behavior although the fitting lines do not pass at the zero point. The threshold voltage extrapolated from both the *J-V* curve is regarded to be ~0.07 V. This voltage is speculated to be the necessary voltage for the tunneling of alkyl chains in the FSAM molecule.

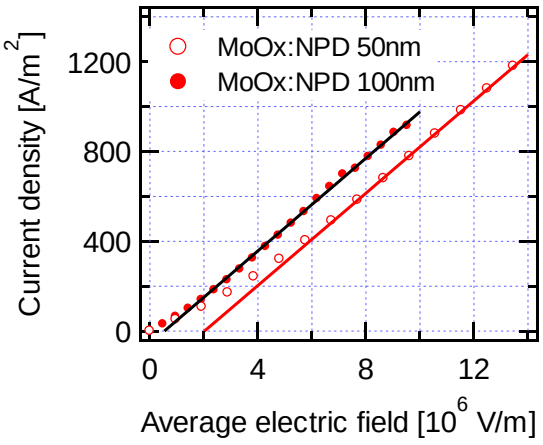

Figure 4-9 Current density-average electric field of the device with a co-evaporation thin film.

Figure 4-9 shows the current density-average electric field of the device with a co-evaporation thin film. Both slopes of *J-E* curves are estimated to be approximately 1.03 x 10^{-4} S/m as shown in Fig. 4-9. Since the conductivity of non-doped tans-poly (acethylene) is almost 10^{-2} S/m, the conductivity of the co-evaporation thin film is not high.

I discuss the carrier density and mobility using the above conductivity of the co-evaporation thin film. In general, current density J is described as $J = qn\mu E$, where q is hole charge, n is carrier density and σ is conductivity.

$$J = qn\mu E \ (\sigma = qn\mu), \quad \ldots (4.5)$$

Since the α-NPD molecule size is almost 1 nm, the molecular density, n can be estimated by

$$n = \frac{N}{V} = \frac{1}{(1\times 10^{-9}[m])^3}, \quad \ldots (4.6)$$

is 10^{27} m^{-3}, where N is the number of α-NPD molecules in a volume V. If all α-NPD molecules are doped by MoO_x at a molar ratio of 1:1, the maximum carrier density of co-evaporation thin film will be 10^{27} m^{-3}. Using the above conductivity and maximum carrier density, the carrier mobility of a co-evaporation thin film is calculated to be 6.44x$10^{-13}$$m^2V^{-1}s^{-1}$. However, as this value is much lower than that of α-NPD, the conduction mechanism of the co-evaporation thin film would become a SCLC model. This does not agree with the experimental result.

If the carrier mobility of the co-evaporation thin film is assumed to be $10^{-4}$$m^2V^{-1}s^{-1}$, which is the same as the minimum mobility of band conduction, the carrier density must be 1.60x10^{18} m^{-3}. This shows that the carrier density of the co-evaporation thin film is much lower than that of conventional organic semiconductor, e.g. CuPc, pemtacene: ~10^{24} m^{-3}. However, this value is higher

than that of the carrier density of 10^{16} m^{-3} with an intrinsic semiconductor, e.g. Si: $1.5x10^{16}$ m^{-3} but lower than that of the carrier density of 10^{20}-10^{21} m^{-3} with an impurity semiconductor. Perhaps the linear *J-V* plot may be caused by both the smooth carrier injection into α-NPD and high carrier density of the bulk.

4-4 Electrical characteristics in co-evaporation thin films of α-NPD and MoOx as a hole injection layer

Figure 4-10 shows the current density-voltage characteristics of the devices with co-evaporation thin films or MoO_x layers. The device consists of [ITO or Ag (20nm)]/[MoO_x: α-NPD(1:1,10nm) or MoOx (10 nm)]/ α-NPD(50nm)/ Alq3(50nm)/LiF(0.6nm)/Al(100nm). Hereafter, the specime is called by the set of anode and hole injection layer, as the other parts are common, e.g. Ag/MoOx, ITO/MoOx:α-NPD.The threshold voltages of current increase are estimated to be approximately 2.4 and 2.1 V, respectively, for the ITO/MoOx:α-NPD and ITO/MoOx. On the other hand, the threshold voltages are estimated to be approximately 2.4 and 2.1V, respectively, for the Ag/MoOx:α-NPD and Ag/MoOx. Although the threshold voltages of current increase for the devices with MoOx:α-NPD thin film are higher than those for the device with MoOx, the voltage of current increase is thought to shift toward the high voltage region because of high current in the low voltage region of <2 V. Therefore, all threshold voltages of current increase are in ~2.1 V, but the current densities of the anode/MoOx:α-NPD are higher than those of the anode/MoOx. This suggests that MoOx:α-NPD enhances hole injection from ITO more than MoOx as a hole injection layer. Probably the current increase will depend on the electron injection from the cathode since an light emission can be observed above the threshold voltage. In the high voltage region above 2 V, the current density of Ag device is higher than that of ITO device and the current density of MoOx:α-NPD device is higher than that of MoOx device.

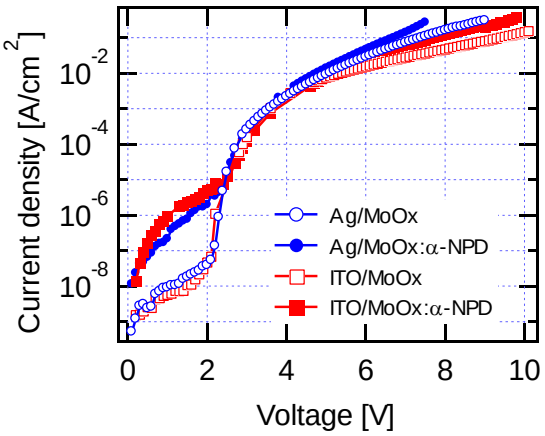

Figure 4-10 Current density–voltage characteristics of the device with a co-evaporation thin film or a MoOx layer. The device structure is ITO or Ag (20nm)/MoO_x:α-NPD(1:1,10nm) or MoO_x(10nm)/α-NPD(50nm)/Alq3(50nm)/LiF(0.6nm)/Al(100nm).

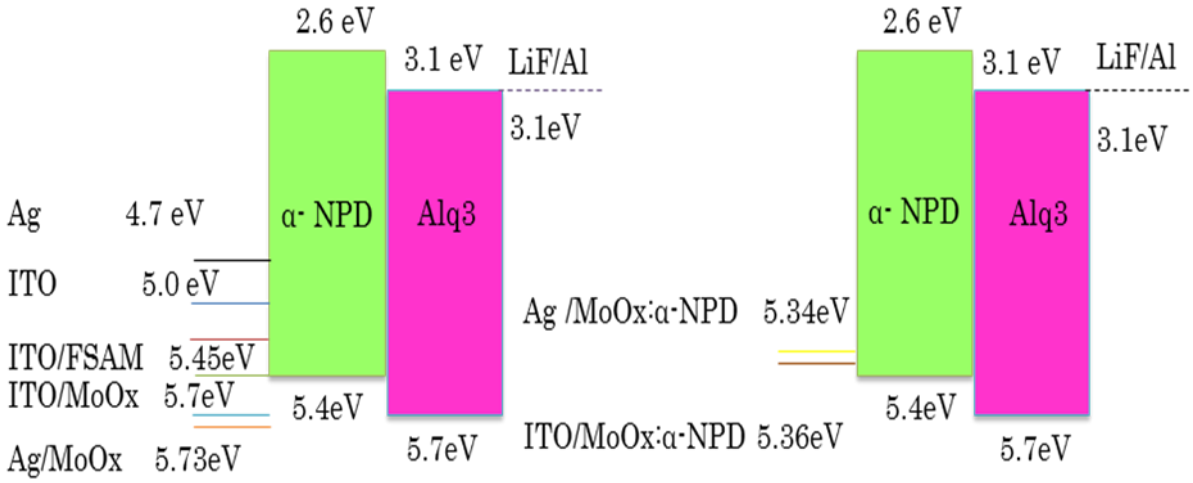

Figure 4-11 Energy diagram of the devices with co-evaporation thin films, MoO_x layers, or FSAM..

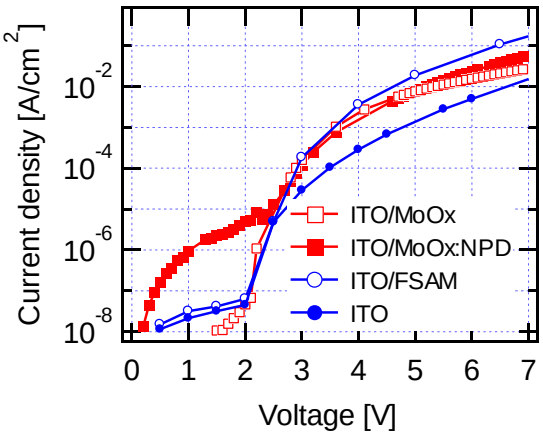

Figure 4-12 Current density–voltage characteristics of the devices with co-evaporation thin films, MoOx layers with or without FSAM. The device structure is ITO /MoO_x:α-NPD(1:1,10nm),MoO_x(10nm), with FSAM or without FSAM/α-NPD(50nm)/Alq3(50nm)/LiF(0.6nm)/Al(100nm).

Figure 4-12 shows the current density-voltage characteristics of the devices with co-evaporation thin films, MoO_x layers with or without FSAM. The device consists of [ITO]/[MoO_x:α-NPD(1:1,10nm), MoOx(10 nm), with or without FSAM]/α-NPD(50nm)/ Alq3(50nm)/LiF(0.6nm)/Al(100nm).The threshold voltages of the ITO, the ITO/FSAM, the ITO/MoOx, and the ITO/MoOx:α-NPD are estimated to be approximately 2.0, 2.0, 2.1, and 2.5 V, respectively. However, the current density of the ITO increases more slowly than those of the other. On the other hand, the current density of the ITO/FSAM increases most remarkabley of the four. Since all potentials of electron injection are thought to be same, the current density of the device is concluded to depend on the hole injection of the anode system.

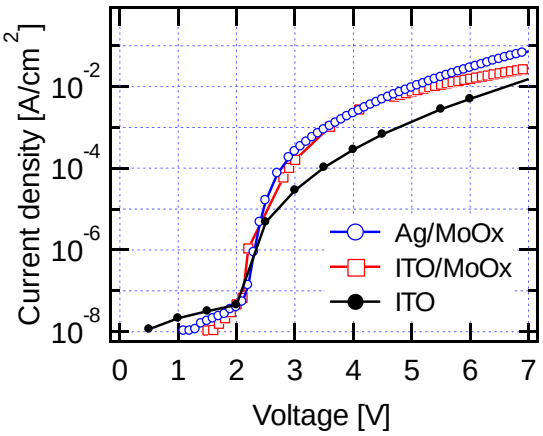

Figure 4-13 Current density–voltage characteristics of the devices of Ag with a MoOx layer, ITO with a MoOx layer or without HIL. The device structure is ITO or Ag (20nm)/MoO_x (10nm) or without HIL/α-NPD(50nm)/Alq3(50nm)/LiF(0.6nm)/Al(100nm).

Figure 4-13 shows the current density-voltage characteristics of the devices of Ag anode with a MoOx layer, ITO anode with a MoO_x layer or without HIL.The device consists of [ITO or Ag(20nm)]/MoOx(10nm) or without HIL]/ α-NPD(50nm)/ Alq3(50nm)/LiF(0.6nm)/Al(100nm). The threshold voltages of the ITO, the the ITO/MoOx, and the Ag/MoOx are estimated to be approximately 2.0, 2.1, and 2.1 V, respectively. Since the current density of the Ag/MoOx is the same as that of the ITO/MoOx, the potential of hole injection of Ag anode is thought to be comparable to that of ITO.

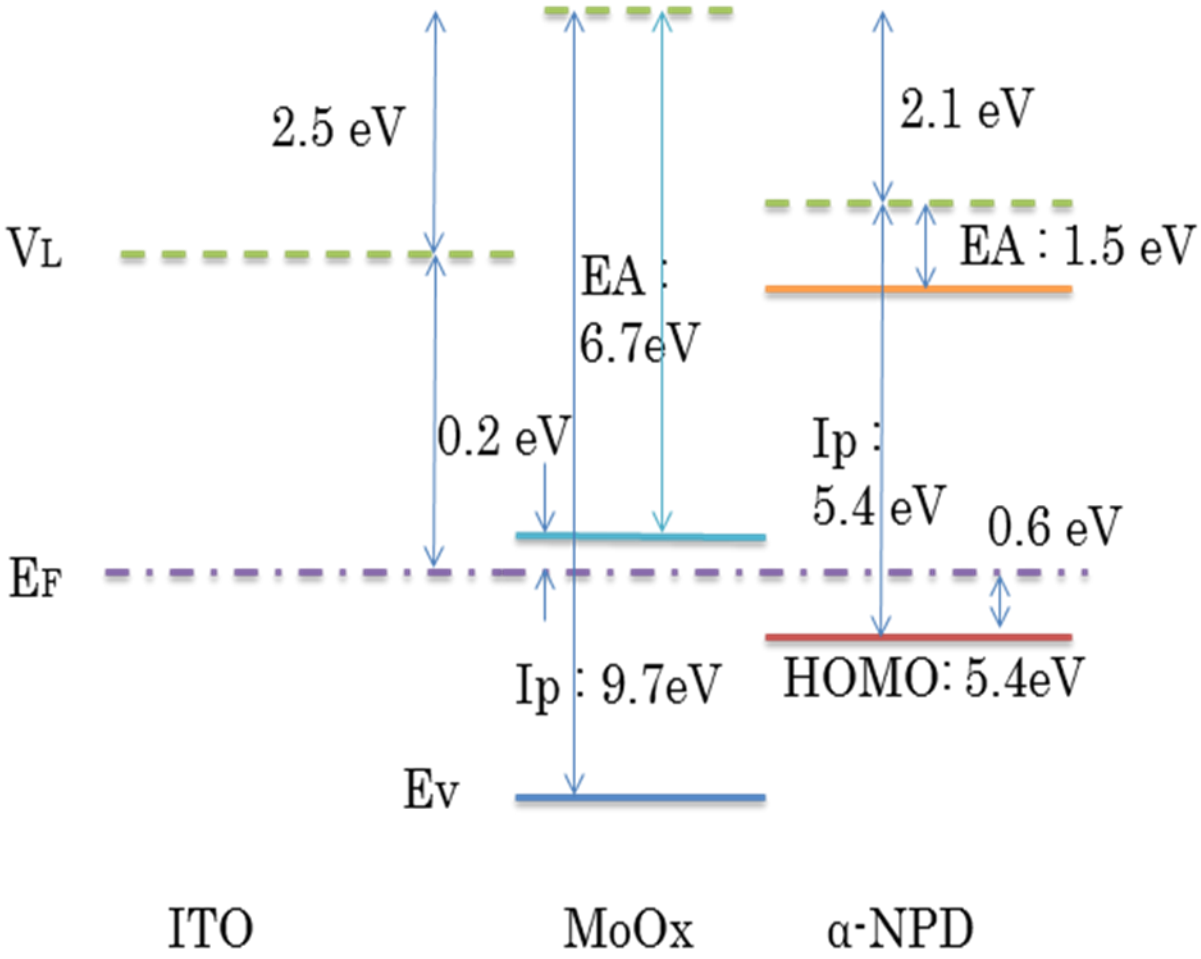

Figure 4-14 Energy level alignment at theMoO_x/α-NPD interface [5,10,11] : V_L is a vacuum level, E_F is the Fermi level, Ip is ion potential, EA is electron affinity, and Ev is a valance band.

The charge transfer between MoOx and α-NPD is depicted as Fig. 4-14. The Fermi level is adjacent to the conduction band for MoOx. The Fermi level is adjacent to the HOMO level for α-NPD. The difference between the HOMO level of α-NPD and the Fermi level of α-NPD is approximately 0.6eV. The difference between the HOMO level of α-NPD and the conduction band of MoOx is approximately 0.8eV [10,11]. Therefore, electrons can be transferred from the HOMO level of α-NPD to the conduction band of MoOx. It is the same as the hole transfer into the HOMO level of α-NPD.

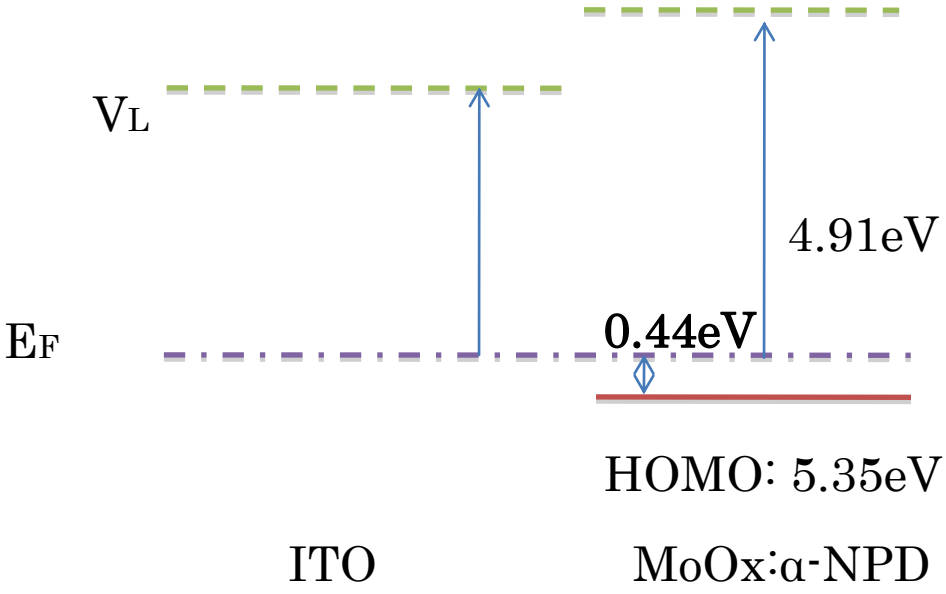

Figure 4-15 Energy level alignment at the co-evaporation thin film of MoOx:α-NPD [5].

The charge transfer mechanism in co-evaporation thin films is as follows. MoOx is thought to act as a p-type dopant to α-NPD. Kröger *et al.* investigated the energy level alignment of MoOx-doped α-NPD thin films. The difference between the HOMO level of a co-evaporation thin film and the Fermi levelof a co-evaporation thin film is dependent on the MoOx doping concentration [11]. The HOMO level of a co-evaporation thin film is adjacent to the Fermi level of a co-evaporation thin film. The difference between the Fermi level of a co-evaporation thin film and the HOMO level of a co-evaporation thin film is reduced by increasing hole densities due to the p-type doping of α-NPD.

4-5 Optical characteristics in co-evaporation thin films of α-NPD and MoOx as a hole injection layer

Figure 4-16 shows the EL efficiency–current density characteristics of the devices with a co-evaporation thin film and a MoOx layer. The maximum EL efficiencies of the

ITO/MoOx:α-NPD and the ITO/MoOx are estimated to be 3.95 and 3.9 cd/A, respectively. On the other hand, those of the Ag/MoOx:α-NPD and the Ag/MoOx are estimated to be 6.8 cd/A and5.5 cd/A, respectively. Although the transmittances of the Ag substrates are lower than those of the ITO substrates as shown in Fig.4-2, the front luminance of the Ag device is higher than that of the ITO device.

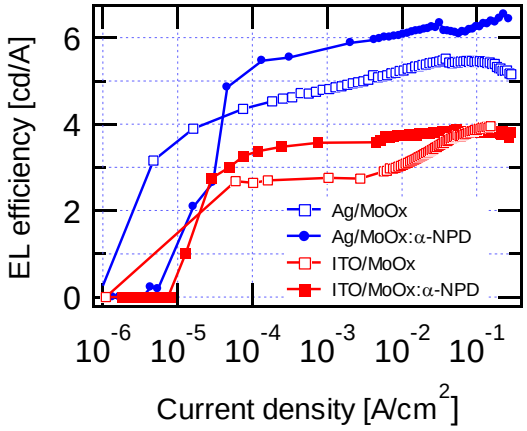

Figure 4-16 EL efficiency - current density characteristics of the devices with a co-evaporation thin film or a MoOx layer as shown in Fig.4-10.

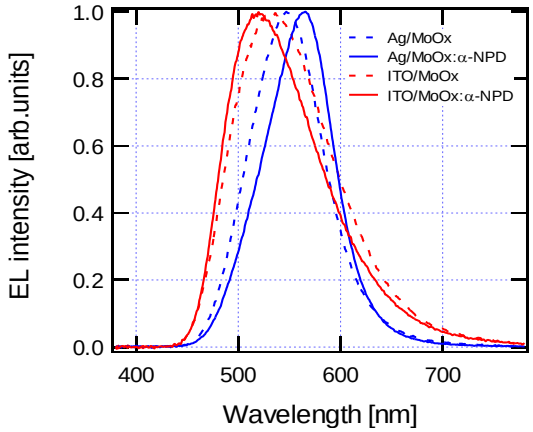

Figure 4-17 EL spectra of the devices with a co-evaporation thin film or a MoOx layer as shown in Fig. 4-10.

Figure 4-17 shows the normalized EL spectra for four different devices at 20 mA/cm^2. The full widths at half maxima (FWHM) of the ITO/MoOx:α-NPD and the ITO/MoOx are estimated to be 106 and 115 nm, respectively. The FWHM of the Ag/MoOx:α-NPD and the Ag/MoOx are estimated to be 80 and 85 nm, respectively. The FWHM of the device with a Ag anode is smaller than that of with ITO. The spectral peaks of the devices with the ITO/MoOx:α-NPD(1:1,10nm), ITO/MoOx (10nm), Ag(20nm)/MoOx(10nm), and Ag(20nm)/MoOx:α-NPD(1:1,10nm) structure are estimated to be 520, 532.5, 547, and 566nm, respectively. The narrowing of FWHM is thought to be due to the microcavity effect.

Peng *et al*. reported that the Ag substrate showes a microcavity structure [12]. A microcavity is a structure formed by reflecting faces on the two sides of a spacer layer or optical medium, and then there is very little this influence between ITO (a transparent) and Al (a reflector). Therefore, the structure between the ITO anode and the Al cathode is not considered as a cavity. Microcavity effect is affected by both the thickness of optical medium and the viewing angle of emission by interference. The EL efficiency of the Ag device can be improved due to the interference phenomena in the microcavity induced by the internal reflection of light between the semitransparent Ag anode and the Al cathode [13]. The Ag/MoOx shows about 41% higher EL efficiency than that of the ITO/MoOx. It is considered that the device can extract strong lights by the microcavity effect between the Al and Ag/MoOx layers based on the low transmittance with an opaque characteristic of the 20nm-thick film Ag. The device with the Ag/co-evaporation thin film shows about 73% higher EL efficiency than that with the ITO/co-evaporation thin film. Therefore, as shown in Fig. 4-20, the EL efficiency of the device with the Ag anode is higher than that of the device with the ITO anode due to increases in the amount of light collected outside of the device by the microcavity effect between the Ag anode and the Al cathode. The EL efficiency of the ITO/MoOx:α-NPD is slightly higher than that of the ITO/MoOx owing to the optical characteristics between the Al and ITO/MoOx:α-NPD with the mismatch possibility of refractive indices at the

interface between air and the ITO/MoOx:α-NPD of low transmittance characteristics. Therefore, the EL efficiency–current density characteristics of the the Ag/MoOx:α-NPD are the highest among the four specimens because of the microcavity effect between Al cathode and Ag anode with the lowest transmittance characteristics.

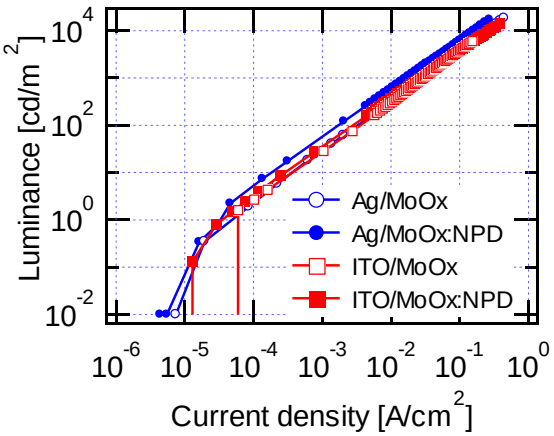

Figure 4-18 Luminance-current density characteristics of the devices with a co-evaporation thin film or a MoOx layer as shown in Fig.4-10.

Figure 4-18 shows the luminance-current density characteristics of the device with a co-evaporation thin film or a MoOx layer as shown in Fig. 4-10.The luminance of the device with the Ag anode and co-evaporation thin film shows the highest value among the used various devices due to the high front luminance characteristics with the Ag/co-evaporation thin film, which exhibits the lowest transmittance.

4-6 Temperature dependence characteristics in co-evaporation thin films

We showed that the introduction of a co-evaporation thin film was effective to improve OLED performance. Therefore, we studied the electrical conduction mechanism of co-evaporation thin films. We investigated the temperature dependence characteristics of co-evaporation thin films

in the temperature range from-100 to 25 ℃.

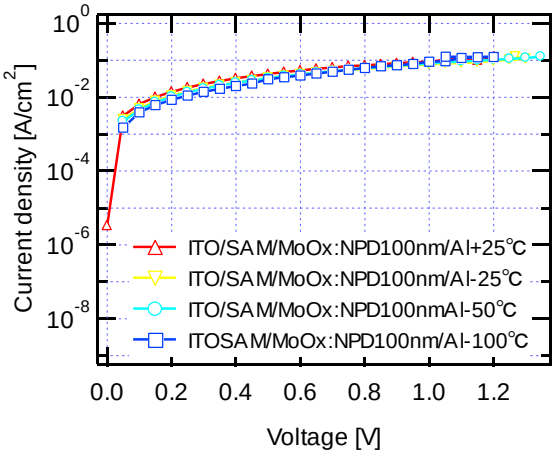

Figure 4-19 Current density-voltage characteristics in co-evaporation thin films at different temperatures

Figure 4-19 shows the current density-voltage characteristics in co-evaporation thin films at different temperatures. The device structure is ITO/FSAM/MoOx:α-NPD (1:1, 100nm)/Al(100nm). The current density-voltage curves are almost same at various temperatures. The device with FSAM did not show temperature dependence characteristics.

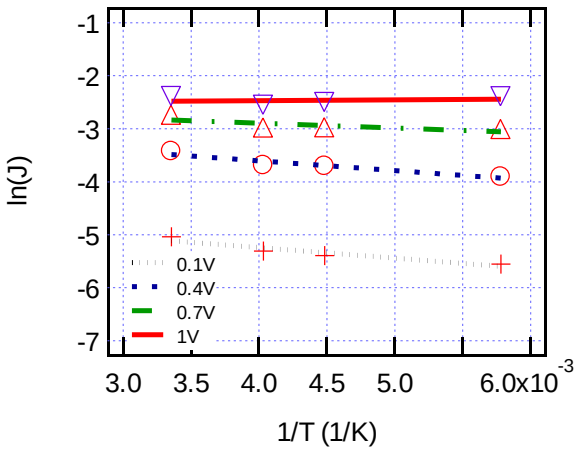

Figure 4-20 Arrhenius plot of the current densities at different temperatures

Figure 4-20 shows the Arrhenius plot of different current densities. Generally, the Arrhenius plots are used to analyze the effects of temperatures on the rates of chemical reactions. We calculated the activation energy based on the Arrhenius plot of the current densities and the Arrhenius formula.

$$J \propto exp(\frac{-E_a}{kT}) \quad \ldots(4.7)$$

where J is the current density [A/cm^2], E_a is the activation energy [eV], k is the Boltzman constant [eV/K], and T is the temperature [K].

The curve fitting is performed with constant voltage intervals (0.3V). The activation energy can be calculated from the slope of *ln*(*J*)-*1/T*. The activation energy calculated from the *ln*(*J*)-*1/T* plot is presented in Table 4-4.

Table 4-4 Equation calculated from the *ln*(*J*)-*1/T* curve

Applied voltage [V]	activation energy [eV]
0.1	0.0171
0.4	0.0158
0.7	0.00803
1	-0.001289

The activation energies are very low. That is, the device with the FSAM and co-evaporation thin film did not show much temperature dependence. The use of a co-evaporation thin film as a hole

injection material in OLED is effective due to the robustness against temperature changes.

4-7 Summary

In Chapter 4, the properties ofthe co-evaporation thin film of MoO_x:α-NPD in OLEDs were examined.

First the ionization potential, transmittance, and surface profile of MoOx: α-NPD thin film were studied and compared with MoOx thin film. As a result, it was shown that MoOx: α-NPD thin film is more suitable than MoOx thin film on the energy matching as a hole injection layer.

Second the electrical properties of MoOx:α-NPD thin film were studied. Since electrical short circuit often ouccrred in the MoOx:α-NPD thin film, FSAM was used as the protect layer aginst electrical short circuit. The conduction mechanism of α-NPD was described as the SCLC model. However, the current density of MoOx:α-NPD thin film was linear to voltage and showed the threshold voltage of 0.07 V. This voltage is thought to be the necessary voltage for the tunneling process between ITO and MoOx:α-NPD thin film. The carrier density of MoOx:α-NPD thin film was estimated by assuming carrier mobility, since the conductivity of MoOx:α-NPD thin film did not depend on thickness of MoOx:α-NPD thin film.

Third MoOx:α-NPD thin film to a hole injection layer was used. Two types of anode, ITO (bottom emission) and Ag (top emmission) was used. The use of MoOx:α-NPD thin film for both anodes was effective for the reduction of driving voltage and high efficiecient performance. Especially the EL efficiency of >6 cd/A was obtained in the device with Ag anode because of the microcavity effect.

References

[1] S. Tokito, K. Noda and Y. Taga, “Metal oxides as a hole-injecting layer for an organic electroluminescent device”, J. Phys. D: Appl. Phys. **29** (1996) 2750.

[2] H. You, Y. Dai, Z. Zhang, and D. Ma, “Improved performances of organic light-emitting diodes with metal oxide as anode buffer”, J. Appl. Phys. **101** (2007) 026105.

[3] A. Kitai, 「Principle of Solar Cells, LEDs and Diodes: The role of the PN junction」, John Wiley & Sons, Ltd. (2011).

[4] S. Tokito and Y. Taga, “Organic electroluminescent devices fabricated using a diamine doped MgF_2 thin film as a hole-transporting layer”, Appl. Phys. Lett. 66 (1995) 6.

[5] M. Kroger, S. Hamwi, J. Meyer, T. Riedl, W. Kowalsky, A. Kahn, “P-type doping of organic wide band gap materials by transition metal oxides: A case-study on Molybdenum trioxide”, Org. Electron. 10 (2009) 932.

[6] T. Matsushima, G. Jin, Y. Kanai, T. Yokota, S. Kitada, T. Kishi, and H. Murata, “Interfacial Charge Transfer and Charge Generation in Organic Electronic Devices Organic Electronics”, Org. Electron. 12 (2011) 520.

[7] Y. S. Park, H. K. Park, J. A. Jeong, K. H. Choi, S. I. Na, D. Y. Kim, and H. K. Kim, “Comparative investigation of transparent ITO/Ag/ITO and ITO/Cu/ITO electrode grown by dual-target DC sputtering for organic photovoltaics” , J. Electrochem. Soc. 156 (2009) 588.

[8] T. Mori, E. Sugimura, T. Mizutani, “Estimate of hole mobilities of some organic photoconducting materials using the time-of-flightmethod”,J. Phys. D : Appl. Phys. 26 (1993) 452.

[9] S. Naka, H. Okada, H. Onnagawa, Y. Yamaguchi, T. Tsutsui, “Carrier transport properties of organic materials for EL device operation”,Synthetic Metals.111–112 (2000) 331.

[10] M. Kröger, S. Hamwi, J. Meyer, T. Riedl, W. Kowalsky, and A. Kahn, “Role of the deep-lying electronic states of MoO3 in the enhancement of hole-injection in organic thin films”,Appl.

Phys. Lett. 95 (2009) 123301.

[11] Y. Yi, S. Cho, and S. Kang, “Comment on “Observation of space-charge-limited current due to charge generation at interface of molybdenum dioxide and organic layer” ”, Appl. Phys. Lett. 97 (2010)016101.

[12] H. J. Peng, X. L. Zhu, J. X. Sun, X. M. Yu, M. Wong, and H. S. Kwok, “Efficiency improvement of phosphorescent organic light-emitting diodes using semitransparent Ag as anode,” Appl. Phys. Lett. **88** (2006) 033509.

[13] J. Cao , X. Liu, M.A. Khan, W. Zhu, X. Jiang,Z. Zhang, S. Xu, “RGB tricolor produced by white-based top-emitting organic light-emitting diodes with microcavity structure” , Curr. Appl. Phys. **7** (2007) 300–304

Chapter 5 Conclusions

Significance of this study

As described in the chapter 1, the high performance of commercial OLED devices can be achieved by the development of materials and the improvement of device structure. In this dissertation, the optimization of hole injection layer was discussed.

First optimization of the fluorinated SAM (FSAM) as a hole injection layer was studied. Since the enhancement of hole injection between FSAM and ITO is modified by the interface dipole moment of FSAM molecules, the alkyl-chain length dependence of hole injection properties for FSAM was investigated. The increase in the alkyl-chain length did not lead to the improvement of hole injection directly. The computer simulation suggested that the increase in alkyl chain (the number of fluorine atom) does not contribute to the increase in the dipole moment of FSAM molecule. Because each C-F dipole moment ($-CF_2-$) in alkyl chains was canceled. However, the packing of FSAM molecules was improved by the increase in alkyl chain because of self-assembling potential of long alkyl chain. Although holes were easily injected by the use of FSAM, the carrier balance of the device with FSAM did not change and its EL efficiency was the same as that of the device without FSAM. In addition, it was suggested that the FSAM with a long alkyl chain can have the injection rate in accordence with the electron injection rate of LiF/Al. It was found that the formation of transition layer around FSAM in α-NPD layer contributes to improve current transport performance.

We used the F10SAM as a hole injection layer. However, the use of the materials with more than 8 fluorinated carbons will be prohibited in future. This study showed that F8SAM was good enough to improve hole injection and can be used instead of F10SAM.

Second application ofthe MoOx:α-NPD co-evaporation thin film as a hole injection was

studied. The ionization potential of the MoOx:α-NPD thin film is estimated to be ~5.35 eV and the energy difference between ITO and α-NPD disappeared by the insert of the MoOx: α-NPD. The conductivity of the MoOx: α-NPD is $1.03x10^{-4}$ S/m. This was a low value for typical organic semiconductors. The high conductivity of the MoOx:α-NPD was caused by the increase in carrier density due to the charge transfer between MoOx and α-NPD. Consequently, the current density of the ITO/FSAM/MoOx: α-NPD showed an Ohmic-like behavior against voltage. These *J-V* curves were straight lines except for the neibhorhood of origin. The threshold voltage of these lines was thought to be the necessary voltage for tunneling of alkyl chain part. In the top emission type, since some metals are used as the anode, the Ag electrode was compared with the ITO anode. When the MoOx:α-NPD was used as a hole injection layer, not only the increase in current density but also the Ohmic current density below 2 V were observed. The current densities of the devices with the MoOx: α-NPD were higher than those of the devices with the MoOx. The apparent activation energy on the current of the MoOx:α-NPD thin film was very small or almost zero.

The advantage of this study's results

The advantage of FSAM is the reduction of the fabrication process for hole injection layer in the vacuum deposition manufacture process. Because the ITO substrate can be treated by the FSAM vapor treatment before the substrates are conveyed in the vacuum chamber.

On the other hand, the fabrication of MoOx: α-NPD thin film can be co-evaporated by two sources. MoOx only have to be evaporated at the initial stage during fabricating α-NPD thin film. Therefore, since there are no new chamber and no additional process, only little change is necessary in the conventional fabrication process. This study is expected to contribute to achieve high performances without complicated and power comsuming fabrication process and to expand OLED display industries in the world display market.

Future challenges

In conventional organic electroluminescent devices before Tang's paper, it was impossible to easily inject both electrons and holes into an emissive material. However, the combination of carrier injection and transport layers gave the exceptional performance to organic electroluminescent devices. This is "Organic light-emitting diodes, OLEDs". It is often said that the carrier balance factor, which is one of efficiency factor in OLEDs, will decrease by the increase in hole injection. However, our results showed that the carrier balance factor does not decrease if a good electron injection from the cathode is maintained. In multi-layer OLEDs, we insist that the carrier balance is always a unity since both carrier injections are controlled by changing voltage distribution among organic layers. I would like to clarify the carrier balance mechanism of OLEDs on carrier injection. In addition, the enhancement of electron injection from the cathode would like to be achieved by SAM treatment.

Research achievements

Publication

[1] S.-G. Park, M. Imanishi, T. Morimoto, T. Inden, T. Nishikawa and T. Mori, “Interface Phenomena of Self-Assembled Monolayer with Various Alkyl Chain as a Hole-Injection Layer for Organic Light-Emitting Diodes”, Mol. Cryst. Liq. Cryst.**567** (2012) 163.

[2] S.-G. Park, H. Wang and T. Mori, “Effects of Using a Ag Anode with a Co-evaporation thin film of MoOx and α-NaphthylDiamine Derivative in Organic Light-Emitting Diode”,Jpn. J. Appl. Phys. **52** (2013) 052102.

International Conference

[1] “Interface Phenomena of Self-Assembled Monolayer with Various Alkyl Chain as a Hole-Injection Layer for Organic Light-Emitting Diodes”
S.-G. Park, M. Imanishi, T. Nishikawa and T. Mori
6th M&BE6, Sendai, JAPAN (2011).

[2] “Interface phenomena of Self-Assembled Monolayer as a Hole-Injection Layer for Organic Light-Emitting Diodes”
S.-G. Park, M. Imanishi, T. Morimoto, T. Inden, T. Nishikawa and T. Mori
JF-ICOMEP, Kyungju, KOREA (2011).

[3] “Formation of Organic Nanodots Using Diamine Derivative and Self-Assembled

Monolayer”

T.Morimoto, S-.G-.Park, T. Inden, T. Nishikawa and T. Mori

SSDM, Nagoya, JAPAN (2011).

[4] “Effect of Self-Assembled Monolayer on Polymer and Organic Light-Emitting Diodes”

S-.G-.Park, M. Imanishi, T.Morimoto, T. Inden, T. Nishikawa and T. Mori

ISEIM, Kyoto, MVP2-16, (2011) pp,110-111

[5] “Effects of Using a Co-evaporation Layer of MoOx and α-NPD in Organic Light-Emitting Diodes”

S-.G-.Park, H. Wang, K. Imai, T.Morimoto, T. Inden, S. Ochiai and T. Mori

ISOME, tokyo, (2012) pp.58-59

[6] “Effect of a Co-evaporation Layer of MoOx and a-NaphthylDiamine Derivative for Organic Light-Emitting Diode”,T. Mori, S.-G. Park, H. Wang

The 4th Int’l Symp. On Organic and inorganic Electronic Materials and Related Nanotechnologies, Kanazawa, Japan, June 17-20 (2013) P2-9

Domestic Conference

[1] “ITO/SAM 陽極の正孔注入性と α-NPD 層挿入の効果”

朴　相建, 今西雅人, 富成征弘, 西川尚男, 森　竜雄

第 58 回応用物理学関係連合講演会, Tokyo (2011)

[2] “多結晶化したα-NPD超薄膜の挿入による正孔注入向上”

森本拓也, 今西雅人, 朴　相建, 森　竜雄

第58回応用物理学関係連合講演会, Tokyo (2011)

[3] “アルキル鎖の異なるフッ素化自己組織化単分子膜によるキャリア注入と界面現象”

位田友哉, 佐藤敏一, 朴　相建, 西川尚男, 森　竜雄

第15回有機EL討論会島根県松江市(2011.11)

Acknowledgments

First of all, I would like to sincerely thank my original supervisor, Professor Tatsuo Mori, who has shared his perspectives on the area of Organic Light-Emitting Diode and who taught me how to bring out the main theme of a research.

I am grateful to my current supervisor, Professor Akimori Tabata, for his enthusiasm for all aspects of his helpful assistance. I also wish to thank Professor YasuoSuzuoki and Satoshi Iwata for many helpful discussions during my study and for critical reading of the manuscript of this dissertation. I would like to thank Professor ShizuyasuOchiai at Aichi Institute of Technology for his valuable advice.

I would like to thank Toshikazu Satoh at Toyota Central R&D Laboratories for fabrication and characterization of samples, and helpful comments.

I should also thank my fellow group members for their friendship and inspiration: Masato Imanishi, Haiying Wang, Takuya Morimoto, TomoyaInden and KazuhiImai and so on.

Finally, I would like to thank my parents and family for their support and patience. Last but not least, special thanks to Min-Kyung, Kim for her encourage and love in the last years.